

Cosmic Infrared Background anisotropies as a window into primordial non-Gaussianity

Marco Tucci^{*}, Vincent Desjacques[†] and Martin Kunz[‡]

*Département de Physique Théorique and Center for Astroparticle Physics (CAP), University of Geneva,
24 quai Ernest Ansermet, CH-1211 Geneva, Switzerland*

ABSTRACT

The angular power spectrum of the cosmic infrared background (CIB) is a sensitive probe of the local primordial bispectrum. CIB measurements are integrated over a large volume so that the scale dependent bias from the primordial non-Gaussianity leaves a strong signal in the CIB power spectrum. Although galactic dust dominates over the non-Gaussian CIB signal, it is possible to mitigate the dust contamination with enough frequency channels, especially if high frequencies such as the *Planck* 857 GHz channel are available. We show that, in this case, measurements of the cosmic microwave background from future space missions should be able to probe the local bispectrum shape down to an amplitude $|f_{\text{NL}}| < 1$.

Key words: cosmology: theory, large-scale structure of Universe, inflation

1 INTRODUCTION

Cosmology offers powerful probes of the high-energy physics in the early Universe. One of the most important discriminants is primordial non-Gaussianity (PNG), which can in principle be tested across our entire past light-cone. While standard single-field slow-roll inflationary models generically predict only very low levels of PNG, other scenarios can lead to a much larger non-Gaussianity in the primordial fluctuations (for more details see e.g. Bartolo et al. 2004; Komatsu 2010; Chen 2010; Liguori et al. 2010; Yadav & Wandelt 2010). Constraints or detections of PNG can thus give us insight into the physics at energy scales that are otherwise very difficult to access.

The *Planck* satellite (Planck Collaboration XVII 2015) has already put stringent constraints on primordial non-Gaussianity, but there is still much space for interesting phenomenology, especially if we can access the regime where the amplitude of the PNG is an order of magnitude smaller than the current limits.

While the cosmic microwave background (CMB) observations are nearly cosmic-variance limited and, therefore, will not improve much over the *Planck* constraint, future surveys of the large scale structure (LSS) hold the promise of achieving much tighter limits. Much effort has already been devoted to constrain PNG from a scale dependence in the galaxy bias (Dalal et al. 2008; Matarrese & Verde 2008;

Slosar et al. 2008). Current LSS limits are at the level of the CMB pre-*Planck* constraints (Giannantonio et al. 2014; Leistedt et al. 2014), and they could improve by up to ~ 1 order of magnitude in the not so distant future (Agarwal et al. 2014; de Putter & Doré 2014; Raccanelli et al. 2015; Camera et al. 2015; Alonso & Ferreira 2015; Raccanelli et al. 2015). Further improvements may come from higher-order statistics such as the galaxy bispectrum (see e.g. Scoccamarro et al. 2004; Sefusatti & Komatsu 2007; Jeong & Komatsu 2009), which encodes much more information on the PNG shape than the non-Gaussian bias. The latter is predominantly sensitive to the ‘local’ bispectrum shape, which peaks on squeezed triangles.

Constraints on f_{NL} from future measurements of the non-Gaussian bias will strongly depend on the survey depth and volume (Carbone et al. 2010; Hamaus et al. 2011; de Putter & Doré 2014). Unfortunately, even the forthcoming large scale surveys such as Euclid (Laureijs et al. 2011) or LSST (Abell et al. 2009) will only cover a small fraction of the total comoving volume accessible to us. The cosmic infrared background (CIB) traces the LSS over a much larger comoving volume and, thus, could potentially outperform future galaxy redshift surveys. In this paper we show that the CIB indeed is an excellent probe of primordial non-Gaussianity that allows us, in principle, to reach $|f_{\text{NL}}| < 1$ in the squeezed bispectrum limit. We demonstrate that such an error can be achieved at Fisher matrix level even upon taking into account the signal produced by galactic dust, which is much stronger than the CIB at low multipoles. However, it is essential to have CIB maps available at enough frequencies.

^{*} Email: Marco.Tucci@unige.ch

[†] Email: Vincent.Desjacques@unige.ch

[‡] Email: Martin.Kunz@unige.ch

The paper is organized as follows. We introduce our halo model of the CIB in §2, and present our forecast for a detection of the non-Gaussian bias in the CIB angular power spectrum in §3. We discuss our findings and, in particular, the contamination by galactic dust in §4 and §5 before concluding in §6. Throughout the paper, we adopt the standard Λ CDM cosmological model as measured by *Planck* (Planck Collaboration XVI 2014): $\{\Omega_m, \Omega_\Lambda, \Omega_b h^2, \sigma_8, h, n_s\} = \{0.3183, 0.6817, 0.02205, 0.8347, 0.6704, 0.9619\}$.

2 MODEL OF THE COSMIC INFRARED BACKGROUND

2.1 Halo model of the CIB intensity

In the usual Newtonian treatment, the observed CIB brightness is given by

$$I(\nu, \hat{n}) = \int_0^{\chi_*} dz \left(\frac{d\chi}{dz} \right) W_\nu^{(\text{CIB})}(z) (1 + \delta_j) \quad (1)$$

where the integral runs over the (unperturbed) comoving distance χ along the line of sight. It is typically computed up to redshift $z_* \sim 10$, corresponding to a comoving distance $\chi_* = \chi(z_*)$, because of the negligible contribution of CIB fluctuations at higher redshifts. The redshift weight for CIB fluctuations is

$$W_\nu^{(\text{CIB})}(z) = a(z) \bar{j}_\nu(z), \quad (2)$$

where $a(z)$ is the scale factor and $\bar{j}_\nu(z)$ is the mean CIB emissivity per comoving volume at frequency ν :

$$\bar{j}_\nu(z) = \int_0^{\bar{L}_{(1+z)\nu}^{\text{cut}}} dL \bar{n}_g(L, z) \frac{L_{(1+z)\nu}}{4\pi}. \quad (3)$$

Here, $\bar{n}_g(L, z)$ denotes the infrared galaxy luminosity function and $L_{(1+z)\nu}$ is the infrared luminosity (in W Hz^{-1}) at the rest-frame frequency $(1+z)\nu$. In practice, only faint sources below the flux detection limit S_{ν}^{cut} are included in the CIB, such that the integral in Eq. (3) is cut off at a (redshift and frequency dependent) luminosity $\bar{L}_{(1+z)\nu}^{\text{cut}}(z)$. The brighter sources are detected and removed from the sky maps. Finally, $\delta_j \equiv \delta_j(\nu, z, \mathbf{x} = \chi(z)\hat{n})$ is the perturbation to the CIB emissivity at frequency ν , redshift z and comoving position $\mathbf{x} = \chi(z)\hat{n}$ along the line of sight.

Let us focus first on the contribution from the average emissivity. Following Shang et al. (2012), we split the mean emissivity into a sum of two contributions,

$$\bar{j}_\nu(z) = \int dM \bar{n}_h(M, z) [f_\nu^c(M, z) + f_\nu^s(M, z)], \quad (4)$$

where the average emissivity produced by the central and satellite galaxies of a given halo at redshift z are

$$f_\nu^c(M, z) = \frac{1}{4\pi} N_c L_{c,(1+z)\nu}(M, z) \quad (5)$$

$$f_\nu^s(M, z) = \frac{1}{4\pi} \int dm \bar{n}_s(m, z|M) L_{s,(1+z)\nu}(m, z). \quad (6)$$

In the above expressions, $\bar{n}_h(M, z)$ and $\bar{n}_s(m, z|M)$ are the halo and sub-halo mass functions, and M and m are the parent halo and sub-halo masses. The numbers N_c of central galaxies is specified by the halo occupation distribution (HOD; Berlind & Weinberg 2002; Zheng et al. 2005). Numerical simulations indicate that N_c typically follows a step-like

function (Kravtsov et al. 2004). We adopt a characteristic mass M_{cen} of the step function of $3 \times 10^{11} M_\odot/h$ (Zehavi et al. 2011; Desjacques et al. 2015), ignoring any luminosity dependence. In all subsequent calculations, we use the SO (Spherical Overdensity) halo and sub-halo mass functions provided by Tinker et al. (2008) and Tinker & Wetzel (2010), respectively, and integrate the sub-halo mass function from a minimum halo mass $M_{\text{min}} = 10^{10} M_\odot/h$ to the parent halo mass M . To identify halos, we adopt a density threshold of $\Delta_c = 200$ (in unit of the background density $\bar{\rho}_m(z)$) at all redshifts.

In the model used here, the luminosity and clustering of infrared galaxies are linked to the host halo mass. The strongly clustered galaxies are situated in more massive halos. They typically have more stellar mass and, therefore, are more luminous. Assuming the same luminosity-mass relation for both central and satellite galaxies, we relate the galaxy infrared luminosity to the host halo mass through the parametric relation (Shang et al. 2012)

$$L_{(1+z)\nu}(M, z) = L_0 \Phi(z) \Sigma(M) \Theta_{\text{CIB}}[(1+z)\nu]. \quad (7)$$

As regards to the luminosity-mass relation, we shall follow the assumptions used in Planck Collaboration XXX (2014):

- L_0 is an overall normalisation that is constrained from measurements of CIB power spectra. In principle, it should be a constant but, in order to have a good fit to Planck Collaboration XXX (2014), we allow small variations of L_0 with the frequency, which are at most a 10 per cent between 217 and 857 GHz.

- The term $\Phi(z)$ describes the redshift-dependence of the normalisation. We adopt a power-law scaling

$$\Phi(z) = (1+z)^\delta.$$

- We assume a log-normal distribution for the dependence $\Sigma(M)$ of the galaxy luminosity on halo mass:

$$\Sigma(M) = \frac{M}{\sqrt{2\pi\sigma_{L/M}^2}} e^{-[\log(M) - \log(M_{\text{eff}})]^2 / 2\sigma_{L/M}^2}, \quad (8)$$

where M_{eff} characterises the peak of the specific IR emissivity and $\sigma_{M/L}$ describes the range of halo masses that produces a given luminosity L , which is fixed to $\sigma_{M/L}^2 = 0.5$.

- For the galaxy spectral energy distribution (SED), we assume a modified blackbody shape with a power-law emissivity as in Hall et al. (2010),

$$\Theta_{\text{CIB}}(\nu) = \begin{cases} (\nu/\nu_0)^\beta B_\nu(T_d)/B_{\nu_0}(T_d) & \nu \leq \nu_b \\ (\nu/\nu_0)^{-\gamma} & \nu > \nu_b \end{cases}, \quad (9)$$

where $B_\nu(T)$ is the brightness of a blackbody with temperature T at the frequency ν , and ν_0 is a reference frequency. The dust temperature T_d is assumed to be a function of redshift according to $T_d = T_0(1+z)^\alpha$. The grey-body and power-law connect smoothly at the frequency ν_b , at which the condition $\text{dln}\Theta(\nu, z)/\text{dln}\nu = -\gamma$ is satisfied. For our fiducial parameters, ν_b is always larger than 3000 GHz, and hence the parameter γ has small relevance in the frequency range we are interested in.

For our fiducial halo model parameters, we adopt the values found in Planck Collaboration XXX (2014) by fitting (auto- and cross-) power spectra of the CIB anisotropies measured by *Planck* and *IRAS* at 217, 353, 545, 857 and 3000 GHz (see Table 1).

Table 1. Fiducial values of the parameters found by [Planck Collaboration XXX \(2014\)](#) for the luminosity-mass relation of the halo model.

α	T_0 [K]	β	γ	δ	$\log(M_{\text{eff}})$ [M_\odot]	L_0 [W Hz^{-1}]
0.36	24.4	1.75	1.7	3.6	12.6	$0.95\text{--}1.05 \times 10^{-3}$

We now turn to the fluctuations of the CIB brightness across the sky. In the Limber approximation, the angular power spectrum of CIB fluctuations can be written as (e.g., [Knox et al. 2001](#); [Song et al. 2003](#)):

$$C_\ell^{(\text{CIB})}(\nu, \nu') = \int_0^{z^*} dz \left(\frac{d\chi}{dz} \right) \frac{1}{\chi^2} W_\nu^{(\text{CIB})}(z) W_{\nu'}^{(\text{CIB})}(z) \times P_{jj}^{\nu \times \nu'} \left(k = \frac{\ell}{\chi}, z \right). \quad (10)$$

Here, $P_{jj}^{\nu \times \nu'}$ is the cross-power spectrum $\langle \delta_j \delta_j' \rangle$ of fluctuations in emissivity at frequency ν and ν' . $P_{jj}(k, z)$ can be set equal to the 3D power spectrum of galaxies, $P_{\text{gg}}(k, z)$, under the assumption that fluctuations in the emissivity trace those of the sources. In the context of the halo model ([Scherer & Bertschinger 1991](#); [Seljak 2000](#); [Scoccimarro et al. 2001](#); [Cooray & Sheth 2002](#)), galaxy power spectra are the sum of the contribution of the clustering in one single halo (1-halo term) and in two different halos (2-halo term):

$$P_{\text{gg}}^{\nu \times \nu'}(k, z) = P_{\text{gg}}^{1h}(k, z, \nu, \nu') + P_{\text{gg}}^{2h}(k, z, \nu, \nu'), \quad (11)$$

where

$$P_{\text{gg}}^{1h}(k, z, \nu, \nu') = \frac{1}{\bar{j}_\nu \bar{j}_{\nu'}} \int dM \frac{dN}{dM} \left[f_\nu^c(M, z) f_{\nu'}^s(M, z) u(k, z|M) + f_{\nu'}^c(M, z) f_\nu^s(M, z) u(k, z|M) + f_\nu^s(M, z) f_{\nu'}^s(M, z) u^2(k, z|M) \right],$$

$$P_{\text{gg}}^{2h}(k, z, \nu, \nu') = \frac{1}{\bar{j}_\nu \bar{j}_{\nu'}} D_\nu(k, z) D_{\nu'}(k, z) P_{\text{lin}}(k, z), \quad (12)$$

and

$$D_\nu(k, z) = \int dM \frac{dN}{dM} b_1(M, z) u(k, z|M) \times \left[f_\nu^c(M, z) + f_\nu^s(M, z) \right]. \quad (13)$$

Here, $u(k, z|M)$ is the normalised Fourier transform of the NFW density profile ([Navarro et al. 1997](#)), $P_{\text{lin}}(k, z)$ is the linear mass power spectrum extrapolated to redshift z , and b_1 is the (Eulerian) linear halo bias (we use the fitting formula given in [Tinker et al. 2010](#)). In principle, $P_{jj}(k, z)$ receives also a shot noise contribution, but we will ignore it as it is typically of the same order as the 1-halo term.

At very large scales, i.e. at multipole $\ell \lesssim 10$, the Limber approximation used in Eq. (10) is not valid. Assuming a negligible contribution from the 1-halo term, for angular scales ranging from $\ell = 2$ to 40 CIB power spectra can be

computed by ([Curto et al. 2015](#))

$$C_\ell^{(\text{CIB})}(\nu, \nu') = \frac{2}{\pi} \int dk k^2 \times \int_0^{z^*} dz \left(\frac{d\chi}{dz} \right) W_\nu^{(\text{CIB})}(z) j_\ell(k\chi(z)) P_{\text{gg}}^{1/2}(k, z, \nu) \times \int_0^{z^*} dz' \left(\frac{d\chi}{dz'} \right) W_{\nu'}^{(\text{CIB})}(z') j_\ell(k\chi(z')) P_{\text{gg}}^{1/2}(k, z', \nu'), \quad (14)$$

where $j_\ell(x)$ are spherical Bessel functions.

2.2 GR corrections and non-Gaussian bias

There are two important ingredients which we wish to add to the above model: General relativistic corrections and non-Gaussian bias. Details about the calculation of the GR effects, which have already been considered in the context of intensity mapping by [Hall et al. \(2013\)](#); [Alonso et al. \(2015\)](#), can be found in Appendix §A2.

At first order in GR perturbations, the observed CIB specific intensity Eq. (1) eventually reduces to

$$I(\nu, \hat{n}) = \int_0^{z^*} dz \left(\frac{d\chi}{dz} \right) W_\nu^{(\text{CIB})}(z) \times \left(1 + \delta_j + \frac{\partial \ln \bar{j}_\nu}{\partial \eta} \delta \eta + \delta_\parallel + 2s \delta_\perp \right), \quad (15)$$

where δ_j is the perturbation to the galaxy emissivity in the source rest-frame and at constant line-of-sight comoving distance χ , the term proportional to $\delta \eta$ arises from the transformation to constant observed redshift, δ_\parallel is the perturbation to the source volume along the line-of-sight, and the term proportional to δ_\perp represents the perturbation to the limiting luminosity generated by fluctuations in the luminosity distance. Note that we have introduced a magnification bias

$$s(z) = \frac{\partial \ln \bar{j}_\nu}{\partial \bar{L}_{(1+z)\nu}^{\text{cut}}} = \frac{\bar{L}_{(1+z)\nu}^{\text{cut}}}{4\pi} \frac{\bar{n}_g}{\bar{j}_\nu} \quad (16)$$

in analogy with source number counts ([Broadhurst et al. 1995](#)). The mean comoving emissivity \bar{j}_ν is given by Eq. (3). In the conformal Newtonian gauge adopted for the calculation, the perturbation to the conformal time η reads

$$\mathcal{H} \delta \eta = -\Psi - \int_0^\chi d\chi' (\dot{\Psi} + \dot{\Phi}) + \mathbf{v} \cdot \hat{\mathbf{n}} \quad (17)$$

while the perturbations to the source volume element parallel and transverse to the beam are

$$\delta_\parallel = \left(\mathcal{H} - \frac{\dot{\mathcal{H}}}{\mathcal{H}} \right) \delta \eta + \Psi + \mathbf{v} \cdot \hat{\mathbf{n}} + \frac{1}{\mathcal{H}} \left[\frac{d\Psi}{d\chi} + (\dot{\Psi} + \dot{\Phi}) - \frac{d\mathbf{v}}{d\chi} \cdot \hat{\mathbf{n}} \right], \quad (18)$$

and

$$\delta_\perp = \mathcal{H} \delta \eta - \frac{1}{\chi} \left[\delta \eta - \int_0^\chi d\chi' (\Psi + \Phi) \right] - \Phi - \kappa, \quad (19)$$

respectively. Here, overdots designate a partial derivative w.r.t. the unperturbed conformal time η . Note that χ and η are related through $\chi = \eta_0 - \eta$. Furthermore,

$$\kappa = \frac{1}{2} \int_0^\chi d\chi' \frac{\chi - \chi'}{\chi \chi'} \nabla_\Omega^2 (\Psi + \Phi), \quad (20)$$

where ∇_Ω^2 is the Laplacian on the unit sphere, is the lensing

convergence. We have restricted ourselves to adiabatic scalar perturbations. There would be more terms, should vector or tensor perturbations or isocurvature modes be present at an appreciable level.

Assuming that spatial variations in the comoving emissivity trace fluctuations in the galaxy number density, intrinsic perturbations to the comoving emissivity δ_j in the Newtonian gauge are related to matter fluctuations δ_m^{syn} in a synchronous gauge comoving with dark matter through (Challinor & Lewis 2011; Baldauf et al. 2011; Jeong et al. 2012)

$$\delta_j = b_1 \delta_m^{\text{syn}} + \frac{\partial \ln \bar{j}_\nu}{\partial \eta} \frac{v}{k}, \quad (21)$$

where $b_1(k) = b_1^{\text{G}}(k) + \Delta b_1^{\text{NG}}(k)$ is the linear galaxy bias. We have written $b_1(k)$ as generally the sum of a Gaussian piece $b_1^{\text{G}}(k)$ (which, in the halo model, depends on wavenumber through the profile $u(k, z|M)$) and a scale-dependent correction $\Delta b_1^{\text{NG}}(k)$ induced by the primordial non-Gaussianity. Furthermore, v is a scalar function such that the (curl-free) velocity perturbation is $\mathbf{v} = k^{-1} \nabla v$ in the Newtonian gauge. Finally, we have ignored the shot-noise contribution for the reasons stated above. Note that Eq. (21) is linear and, thus, corresponds to our halo bias $b(M, z)$ in Eq. (13).

To relate the perturbations Ψ , Φ , δ_m^{syn} and v to the initial conditions, we use $\Phi_i(\mathbf{k}) = (3/5)\zeta(\mathbf{k})$, where $\zeta(\mathbf{k})$ is the uniform-density gauge curvature perturbation on super-horizon scales (i.e. $k \ll \mathcal{H}$), as a reference. Our choice follows from the fact that, in the large scale structure literature, the primordial non-Gaussianity is commonly laid down immediately after matter-radiation equality (see, e.g., Desjacques & Seljak 2010, for a review), whence the factor of 3/5. The various transfer functions will generally depend on the matter content of the Universe. Ignoring anisotropic stresses, these are given by

$$T_\Psi(k, z) = g(z)T(k) \quad (22)$$

$$T_\Phi(k, z) = T_\Psi(k, z)$$

$$T_\delta(k, z) = \frac{2}{3\Omega_m} \left(\frac{k}{\mathcal{H}_0} \right)^2 T(k)D(z)$$

$$T_v(k, z) = \left(\frac{\mathcal{H}}{k} \right) f T_\delta(k, z).$$

Here and henceforth, $g(z)$ and $D(z) = a(z)g(z)$ are the growth function of potential and density perturbations, respectively, f is the logarithmic derivative $f = d \ln D / d \ln a$ and the matter transfer function $T(k)$ is obtained with the Boltzmann code CAMB in a synchronous gauge comoving with the pressureless matter. Note that, with our definitions, the Fourier modes of the peculiar velocity \mathbf{v} are given by $\mathbf{v}(\mathbf{k}, z) = i\mathbf{k}\mathcal{H}fT_\delta(k, z)\Phi_i(\mathbf{k})/k^2$.

Non-Gaussianity generated outside the horizon induces a 3-point function that is peaked on squeezed or collapsed triangles for realistic values of the scalar spectral index. The resulting non-Gaussianity depends only on the local value of the curvature perturbation, and can thus be conveniently parameterized by $\Phi_i = \phi + f_{\text{NL}}(\phi^2 - \langle \phi^2 \rangle)$, where ϕ denotes a Gaussian field (Salopek & Bond 1990; Gangui et al. 1994). The quadratic term introduces a coupling between short- and long-wavelength modes, which results in a scale-

dependent halo bias at large scales (Dalal et al. 2008; Matarrese & Verde 2008). This non-Gaussian bias takes the form (Slosar et al. 2008)

$$\Delta b_1^{\text{NG}}(k, z) = 3f_{\text{NL}} \left(\frac{\partial \ln \bar{n}_h}{\partial \ln \sigma_8} \right) \frac{\Omega_m \mathcal{H}_0^2}{a(z) T_\Phi(k, z) k^2}. \quad (23)$$

It is this bias enhancement on large scales that we are trying to measure with the CIB. A large, potentially detectable $f_{\text{NL}} \gtrsim 1$ can be produced e.g. by multiple scalar fields (Linde & Mukhanov 1997; Lyth et al. 2003).

We have assumed that the halo mass function is universal and, thus, replaced the logarithmic derivative of the mass function by $\delta_c(b_1(M, z) - 1)$, where $\delta_c \sim 1.68$ is the present-day (linear) critical density threshold. For the linear Gaussian bias, we use the fitting formula given in Tinker et al. (2010).

Departure from Statistical Gaussianity in the initial conditions significantly affect the abundance of highly biased tracers of the LSS, since their frequency sensitively depends on the tail of the density PDF (e.g. Lucchin & Matarrese 1988). To ascertain the importance of this effect, we have replaced the halo mass function in Eq. (4) by

$$\bar{n}_h(M, z, f_{\text{NL}}) = \bar{n}_h^{\text{G}}(M, z) \left(1 + R(M, z, f_{\text{NL}}) \right), \quad (24)$$

where $\bar{n}_h^{\text{G}}(M, z)$ is our fiducial Gaussian, Tinker mass function and $R(M, z, f_{\text{NL}})$ is the non-Gaussian fractional correction modelled along the extensions proposed by Matarrese et al. (2000); Lo Verde et al. (2008) (see Desjacques & Seljak (2010) for a discussion). We have found that, for an input value $f_{\text{NL}} = 1$, including $R(M, z, f_{\text{NL}})$ amounts to a $\sim 1\%$ correction to the amplitude of the non-Gaussian CIB bias. We will thus ignore this effect in what follows.

2.3 Signature of PNG in the CIB anisotropies

The signature imprinted by the scale-dependent, non-Gaussian halo bias is largest at low multipoles where the contribution of the 1-halo term is negligible. We have indeed checked that, for the frequencies considered in our forecast, the 1-halo term is at most $\lesssim 10\%$ of the 2-halo contribution. This corresponds to an effective nonlinear parameter $|f_{\text{NL}}| \lesssim 0.1$, which is hardly accessible to CMB experiments with the sensitivity considered here. Therefore, we can safely neglect it at the low multipoles $\ell \leq 40$ where Eq. (14) is applied. Notwithstanding, we include it at the higher multipoles used to constrain the CIB model parameters since it dominates over the 2-halo term for $\ell \gtrsim 1000$.

At low multipoles $\ell \lesssim 40$ where the Limber approximation is not valid, we ignore the 1-halo term, but retain the GR corrections and the non-Gaussian bias so that the CIB angular power spectrum is computed as

$$\begin{aligned} C_\ell^{(\text{CIB})}(\nu, \nu') &= \frac{2}{\pi} \int dk k^2 \\ &\times \int_0^{z^*} dz \left(\frac{d\chi}{dz} \right) W_\nu^{(\text{CIB})}(z) F_\ell(\nu, k, \chi(z)) P_{\Phi_i}^{1/2}(k) \\ &\times \int_0^{z'^*} dz' \left(\frac{d\chi'}{dz'} \right) W_{\nu'}^{(\text{CIB})}(z') F_\ell(\nu', k, \chi(z')) P_{\Phi_i}^{1/2}(k). \end{aligned} \quad (25)$$

Here, $P_{\Phi_i}(k)$ is the power spectrum of our reference curvature perturbation, and is related to the linear matter power

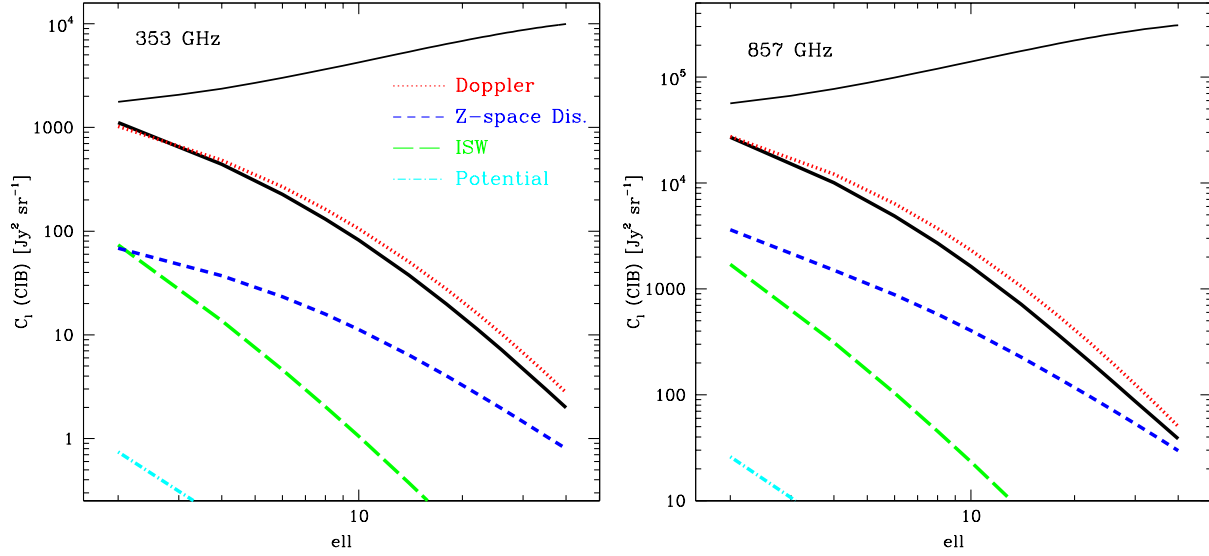


Figure 1. GR corrections (solid thick lines) to the CIB power spectrum (solid thin lines) at 353 (left panel) and 857 GHz (right panel). The different GR contributions are also isolated: the velocity term (dotted red lines); the redshift–space distortion (short dashed blue lines); the ISW term (long dashed green term); the potential term (dot–dashed cyan lines). The GR corrections are relevant at the very first multipoles, and become lower than 1 per cent at $\ell > 10$. The dominant contribution comes from the velocity term.

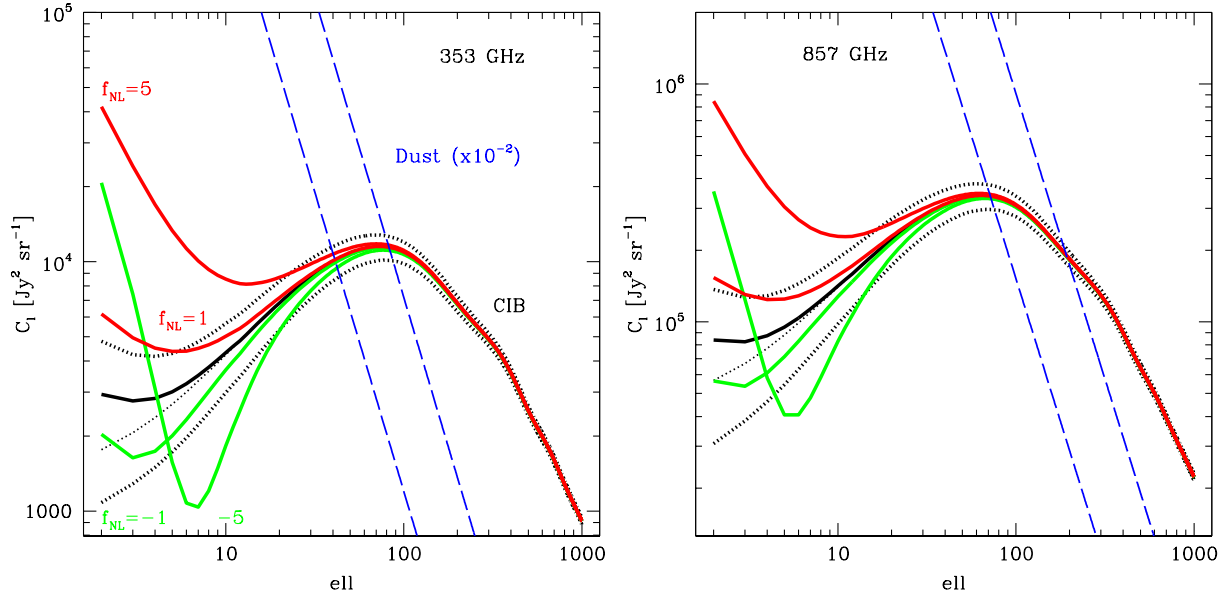


Figure 2. CIB power spectra (including GR corrections) at 353 and 857 GHz assuming Gaussian primordial fluctuations (black solid lines) and $f_{\text{NL}} = \pm 1$ and ± 5 (solid red and green lines). The two, upper and lower thick dotted lines indicate the cosmic variance associated to the Gaussian case, whereas the median, thin dotted curve is the CIB power spectrum without the GR corrections. Also shown as blue dashed line is the dust contamination – reduced by a factor 100 – as measured by [Planck Collaboration XXII \(2015\)](#) for the cleanest sky patches with coverage fraction 10 (left line) and 40 per cent (right line). The dust contamination is still orders of magnitude larger than CIB fluctuations on large angular scales. At $\ell = 2$ the CIB spectrum increases by about an order of magnitude as we turn on f_{NL} from 0 to ± 5 . At larger multipoles, the effect of non–Gaussianity quickly decreases, and it is lower than cosmic variance at $\ell \gtrsim 20$ even for $f_{\text{NL}} \sim 5$. For negative values of f_{NL} , the CIB power spectrum presents a minimum at $\ell \lesssim 10$ corresponding to the angular scale at which the NG bias contribution becomes dominant over the Gaussian bias term.

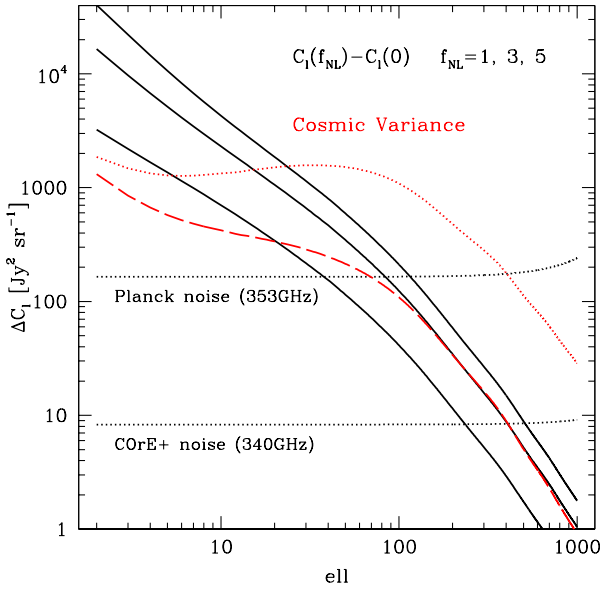


Figure 3. The cosmic variance associated to the CIB power spectrum with Gaussian initial conditions at 353 GHz (red dotted line) is shown in comparison with the PNG signal $\Delta C_\ell = C_\ell(f_{\text{NL}}) - C_\ell(0)$ for $f_{\text{NL}} = 1, 3$ and 5 (black solid lines). The red dashed line gives the cosmic variance reduced by a factor $\sqrt{\ell}$, corresponding to power spectra binned in multipole intervals of size ℓ . The cosmic variance becomes lower than ΔC_ℓ at $\ell \lesssim 20$ for $f_{\text{NL}} = 1$ and lower or equal to ΔC_ℓ up to $\ell \gtrsim 1000$ for $f_{\text{NL}} = 3$. We also plot the noise level for the *Planck* and CORe+ channels at $\nu \sim 350$ GHz (black dotted lines).

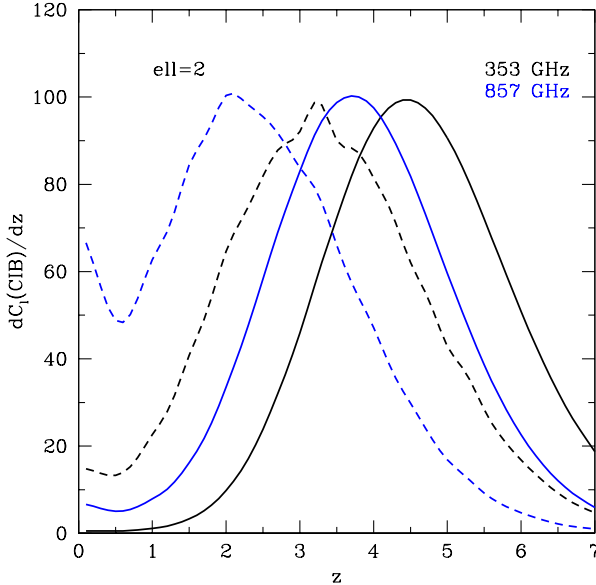


Figure 4. The redshift kernel for the CIB power spectrum at $\ell = 2$ for two different frequencies: 353 GHz (black lines) and 857 GHz (blue lines). Dashed lines are for Gaussian primordial fluctuations, whereas solid lines assume local PNG with $f_{\text{NL}} = 5$. CIB anisotropies induced by PNG mainly arise from dusty galaxies at redshifts between $2.5 \lesssim z \lesssim 6$ with a mild dependence on frequency.

spectrum through

$$P_{\text{lin}}(k, z) = \frac{4}{9\Omega_m^2} \left(\frac{k}{\mathcal{H}_0} \right)^4 T^2(k) D^2(z) P_{\Phi_i}(k). \quad (26)$$

Furthermore, the radial window function $F_\ell(\nu, k, \chi)$ is given by

$$\begin{aligned} F_\ell(\nu, k, z) = & j_\ell(k\chi) \left[b_1(\nu, k, z) T_\delta + \frac{\partial \ln \bar{j}_\nu}{\partial \eta} \left(\frac{T_\nu}{k} - \frac{T_\Psi}{\mathcal{H}} \right) + \frac{\dot{\mathcal{H}}}{\mathcal{H}^2} T_\Psi \right. \\ & + \frac{1}{\mathcal{H}} (\dot{T}_\Psi + \dot{T}_\Phi) \left. \right] + j'_\ell(k\chi) \left[\left(\frac{1}{\mathcal{H}} \frac{\partial \ln \bar{j}_\nu}{\partial \eta} - \frac{\dot{\mathcal{H}}}{\mathcal{H}^2} + 2 \right) T_\nu \right. \\ & + \frac{k}{\mathcal{H}} T_\Psi \left. \right] - j''_\ell(k\chi) \left(\frac{k}{\mathcal{H}} \right) T_\nu - \left(\frac{1}{\mathcal{H}} \frac{\partial \ln \bar{j}_\nu}{\partial \eta} - \frac{\dot{\mathcal{H}}}{\mathcal{H}^2} + 1 \right) \\ & \times \int_0^\chi d\chi' j_\ell(k\chi') (\dot{T}_\Psi + \dot{T}_\Phi), \end{aligned} \quad (27)$$

with the linear bias

$$\begin{aligned} b_1(\nu, k, z) = & \int dM \left[b_1^G(M, z) + 3f_{\text{NL}} \delta_c (b_1^G(M, z) - 1) \frac{\Omega_m \mathcal{H}_0^2}{a T_\Phi k^2} \right] \\ & \times \bar{n}_h(M, z) \left[f_\nu^c(M, z) + f_\nu^s(M, z) \right] u(k, z | M) \end{aligned} \quad (28)$$

predicted by the halo model and including the correction due to primordial non-Gaussianity. Details about the calculation of $F_\ell(\nu, k, z)$ can be found in Appendix §A3. Note that Eq. (27) does not include the lensing magnification induced by the luminosity cut-off, see Eq. (3). The typical flux density cuts in CMB maps indeed are of the order of ≈ 100 mJy, which correspond to luminosities $> 10^{27}$ W Hz $^{-1}$ at $z > 1$. These luminosities are much larger than the expected luminosity of submillimeter galaxies.

In Fig. 1, the GR corrections to the CIB power spectrum are shown at frequency 353 and 857 GHz. As expected, these corrections are relevant only at the very large angular scales, $\ell \lesssim 10$. At $\ell = 2$, they are of the same order of magnitude as the CIB spectrum (assuming Gaussian primordial fluctuations) and decrease to 1–2 per cent at $\ell = 10$, with little dependence on the frequency. GR corrections are dominated by the velocity term, whereas the other terms can be considered negligible¹.

The effect of primordial non-Gaussianity on the CIB power spectrum is much more pronounced than the imprint of GR corrections so long as $|f_{\text{NL}}| \gtrsim 1$. For $|f_{\text{NL}}| \lesssim 1$, the GR corrections must be included in the analysis to avoid significant bias on f_{NL} (see Camera et al. (2015) for related discussion in the context of galaxy redshift surveys). In Figure 2, we compare the CIB spectrum assuming $f_{\text{NL}} = \pm 5, \pm 1$ and 0 , i.e. with primordial Gaussian conditions. GR corrections are also included (see the small increment in CIB spectra with $f_{\text{NL}} = 0$ at the first ℓ s). Like GR corrections, the non-Gaussian bias leads to a pronounced signal at low multipoles ($\ell \lesssim 10$), which decreases proportionally to ℓ^{-1} . Namely, a local PNG with $f_{\text{NL}} \sim 5$ increases the CIB power spectrum by one order of magnitude at $\ell = 2$, and by a factor of $\lesssim 2$ at $\ell = 10$. When $f_{\text{NL}} < 0$, the CIB spectrum has typically less power than in the Gaussian case. It reaches a

¹ In Figure 1, the contribution to GR corrections from a single term are computed neglecting the other components. It should be noted that the total GR correction is not simply the sum of the single contributions because the double products among different terms in Eq. (25) have to be included.

minimum at some multipole (due to a cancellation in the 2-halo term) before increasing again at very low ℓ . This leads to a characteristic feature in the CIB power spectrum.

To gain some insight into the redshift and frequency dependence of the non-Gaussian signal, let us assume that the luminosity-mass relation can be approximated by a Dirac delta, i.e. $\Sigma(M) \approx \delta_D(M - M_{\text{eff}})$. In this case, the non-Gaussian CIB bias $\Delta b_1^{\text{NG}}(\nu, k, z)$ simplifies to

$$\begin{aligned} \Delta b_1^{\text{NG}}(\nu, k, z) &\approx \frac{3}{4\pi} f_{\text{NL}} \frac{\Omega_m \mathcal{H}_0^2}{a T_\Phi k^2} L_0 (1+z)^\delta \Theta_{\text{CIB}}[(1+z)\nu] \\ &\times \frac{\partial}{\partial \ln \sigma_8} \left[\bar{n}_h(M_{\text{eff}}, z) \Theta_H(M_{\text{eff}} - M_{\text{cen}}) \right. \\ &\left. + \int_{M_{\text{eff}}}^\infty dM \bar{n}_h(M, z) \bar{n}_s(M_{\text{eff}}, z|M) \right], \quad (29) \end{aligned}$$

where Θ_H is the Heaviside step function. The integrand of the second term in the square bracket will be maximized for some halo mass $M = \alpha M_{\text{eff}}$ with $\alpha > 1$ and, thus, can be approximated as $\approx \bar{n}_h(\alpha M_{\text{eff}}, z) \bar{n}_s(M_{\text{eff}}, z|\alpha M_{\text{eff}})$. Note that α will generally depend on redshift. A similar calculation yields

$$\begin{aligned} b_1^{\text{G}}(\nu, k, z) &\approx \frac{L_0}{4\pi} (1+z)^\delta \Theta_{\text{CIB}}[(1+z)\nu] \\ &\times \left[\bar{n}_h(M_{\text{eff}}, z) b_1^{\text{G}}(M_{\text{eff}}, z) \Theta_H(M_{\text{eff}} - M_{\text{cen}}) \right. \\ &\left. + \int_{M_{\text{eff}}}^\infty dM b_1^{\text{G}}(M, z) \bar{n}_h(M, z) \bar{n}_s(M_{\text{eff}}, z|M) \right] \end{aligned} \quad (30)$$

for the Gaussian part of the CIB bias. Hence, ignoring the contribution from the satellite galaxies, the relative amplitude of the non-Gaussian CIB bias scales like

$$\begin{aligned} \frac{\Delta b_1^{\text{NG}}}{b_1^{\text{G}}}(\nu, k, z) &\sim 3 f_{\text{NL}} \frac{\Omega_m \mathcal{H}_0^2}{a T_\Phi k^2} (b_1^{\text{G}}(M_{\text{eff}}, z))^{-1} \\ &\times \frac{\partial \ln \bar{n}_h}{\partial \ln \sigma_8}(M_{\text{eff}}, z) \Theta_H(M_{\text{eff}} - M_{\text{cen}}), \end{aligned} \quad (31)$$

i.e. it does not depend on ν . Therefore, the relative amplitude of the signal will weakly depend on the value of δ or the exact shape of Θ_{CIB} which, in our model, do not depend on halo mass. We thus expect that the CIB non-Gaussian bias mainly depends on the HOD parameters, i.e. M_{eff} , M_{cen} and the distribution of subhalos hosting galaxies. We will ascertain the sensitivity to HOD modeling in more detail in §5.

2.4 Galactic dust and cosmic variance

Figure 2 shows the two major constraints for the detection of PNG in CIB spectra: the Galactic dust emission and the cosmic variance. The former dominates the CIB emission at all the relevant frequencies by orders of magnitude, especially on the largest angular scales. Its power spectrum is typically $\propto \ell^{-2.4}$ and the amplitude is strongly dependent on the area of the sky considered. We will extensively discuss this point later in §4. The second main constraint comes from the cosmic variance. We can note that $|f_{\text{NL}}| \gtrsim 1$ is required in order to have corrections to CIB spectra larger than the cosmic variance associated to the ‘‘standard’’ CIB spectrum. The signal is, in any case, tiny already at $\ell \gtrsim 20$ even for larger f_{NL} and typically below the cosmic variance. However, cosmic variance can be significantly reduced by

combining information from independent multipoles. As example, if we assume to measure the CIB power spectra in bins of width ℓ , the cosmic variance will decrease by a factor $\sqrt{\ell}$, as shown in Figure 3. The cosmic variance will be then of the same level as or lower than the PNG signal for $|f_{\text{NL}}| \gtrsim 3$ at all the multipoles considered.

It is well known that the redshift distribution of dusty galaxies which mainly contribute to CIB anisotropies slowly changes with frequency. Namely, it moves to higher redshifts when the CIB is observed at longer wavelengths (e.g., [Planck Collaboration XVIII 2011](#)). For example, we show in Figure 4 the redshift integrand for the CIB spectra at $\ell = 2$: the peak shifts from redshift 2 to ~ 3 when the frequency changes from 857 to 353 GHz. In both cases, however, the contribution from high-redshift galaxies ($z \gtrsim 4$) is not negligible. It is interesting to consider the same in the presence of PNG (in Figure 4, $f_{\text{NL}} = 5$). At $\ell = 2$, where the CIB spectrum is dominated by anisotropies induced by PNG, the integrand peaks even at higher redshifts, i.e. at $z = 3.5$ – 4.5 according to the frequency. CIB anisotropies induced by PNG are therefore mainly from dusty galaxies at redshifts significantly higher than for the ‘‘standard’’ CIB, covering a redshift interval between $2 \lesssim z \lesssim 7$.

3 FISHER MATRIX FORMALISM

We adopt a Fisher matrix approach to provide estimates of the sensitivity of CIB measurements to primordial non-Gaussianity. In terms of power spectra, the Fisher matrix element F_{ij} can be written as (e.g., [Tegmark et al. 2000](#))

$$F_{ij} = \sum_{\ell=\ell_{\text{min}}}^{\ell_{\text{max}}} \frac{2\ell+1}{2} f_{\text{sky}} \text{Tr} \left(\mathbf{C}_\ell^{-1} \frac{\partial \mathbf{C}_\ell}{\partial \theta_i} \mathbf{C}_\ell^{-1} \frac{\partial \mathbf{C}_\ell}{\partial \theta_j} \right), \quad (32)$$

The model parameters θ_i and θ_j include the CIB model parameters given in Table 1 plus the primordial non-Gaussianity parameter f_{NL} and, when considered, the parameters related to the dust emission. The covariance matrix \mathbf{C}_ℓ is an $N_\nu \times N_\nu$ matrix whose elements are defined as the auto- and cross-power spectra of data at N_ν different observational frequencies, i.e. $(\mathbf{C}_\ell)_{ij} = C_\ell^{\nu_i \nu_j}$. In absence of residual foregrounds and CMB radiation, $C_\ell^{\nu_i \nu_j} = C_\ell^{(\text{CIB})}(\nu_i, \nu_j) + N_\ell(\nu_i) \delta_{ij}$, where the diagonal elements of the covariance matrix contain the Gaussian instrumental noise terms:

$$N_\ell(\nu) = w_\nu^{-1} \exp \left(\ell(\ell+1) \frac{\theta_{\text{FWHM}}^2(\nu)}{8 \log 2} \right), \quad (33)$$

where $w_\nu^{-1/2}$ is the instrumental white noise level in $\text{Jy sr}^{-1/2}$ and θ_{FWHM} is the full-width at half-maximum beam size in radians at the frequency ν . In Eq. (32), f_{sky} is the fraction of the sky used to recover CIB fluctuations, and the factor $(2\ell+1)f_{\text{sky}}$ gives the effective number of uncorrelated modes per multipole.

The uncertainty on f_{NL} is computed after marginalizing over the other parameters, i.e. upon inverting the Fisher matrix so that $\sigma(f_{\text{NL}}) = \sqrt{[F^{-1}]_{11}}$ (where $i = 1$ in the Fisher matrix corresponds to the f_{NL} parameter). In Eq. (32), we define the smallest observable multipole for an experiment to be $\ell_{\text{min}} = \pi/(2f_{\text{sky}}^{1/2})$, rounding up to the next integer.

Table 2. Uncertainty on f_{NL} obtained from a CORe+–like experiment in purely CIB+noise maps, using 40% of the sky, with different frequency combinations and $\ell_{\text{min}} = 3$ and 20.

#	ν [GHz]	$\sigma(f_{\text{NL}} = 0)$	
		$\ell_{\text{min}} = 3$	$\ell_{\text{min}} = 20$
1	340	0.68	3.0
2	340, 520	0.52	1.4
4	[220, 520]	0.36	0.50
8	[220, 600]	0.21	0.22

As maximum multipole, we assume $\ell_{\text{max}} = 1000$. This guarantees that the shot–noise contribution from star–forming dusty galaxies is negligible. Moreover, multipoles $\ell \gtrsim 1000$ provide negligible information on f_{NL} .

As a first step, we apply the Fisher formalism to the ideal case of CIB maps from which (Galactic) foregrounds and CMB have been perfectly removed. We refer to the instrumental configuration of a possible future CMB mission like CORe+², as reported in Table 4. Hereafter, only frequencies higher than 200 GHz will be considered in the analysis. Channels at lower frequencies are in fact dominated by the CMB and should be dedicated to removing CMB fluctuations from the signal.

This preliminary test gives us an idea of the maximum level at which f_{NL} can be detected through CIB observations by future space missions dedicated to the measurement of the CMB polarization. In Table 2 we report the uncertainty on f_{NL} assuming $f_{\text{NL}} = 0$, using 40% of the sky and a different number of frequencies. $\sigma(f_{\text{NL}})$ is weakly dependent on the value of f_{NL} . We see that, in principle, $|f_{\text{NL}}|$ of 1–2 could be detectable with high significance ($\gtrsim 3\text{-}\sigma$) using 2–4 frequency channels, while $|f_{\text{NL}}|$ lower than 1 is accessible only if $N_\nu > 4$. We also quote the results obtained after neglecting the first 20 multipoles, which are the most affected by Galactic dust residuals. While we observe a strong degradation in the f_{NL} sensitivity when only 1 or 2 frequency channels are employed, the uncertainty on f_{NL} only marginally increases for $N_\nu \geq 4$. This proves that the very large angular scales are not strictly required to detect the PNG signal.

We emphasize that an estimate of CIB fluctuations at different frequencies is crucial to measure f_{NL} . Apart from giving a better control of the foregrounds, it allows 1) a reduction of the noise level by a factor $\approx \sqrt{N_\nu}$ (if all channels have the same sensitivity) and 2) an improvement of the determination of CIB parameters (with $\sigma(f_{\text{NL}}) \rightarrow 1/F_{11}$ for $N_\nu > 2$). In addition, because CIB anisotropies are not perfectly correlated at different frequencies, multi–frequency CIB observations allow to combine signals from partly overlapping volumes of the Universe. In the overlapping regions, these measurements trace similar matter fluctuations. Therefore, they can be combined to decrease cosmic variance and improve the signal-to-noise ratio, analogously to the multi-tracer technique in galaxy clustering (see e.g. Seljak 2009; Hamaus et al. 2011, for applications to f_{NL}).

4 FORECASTS INCLUDING GALACTIC DUST CONTAMINATION

Measuring CIB anisotropies is a challenging task, especially over large areas of the sky, even for future high–sensitivity CMB space missions. CIB fluctuations are a sub–dominant component at all frequencies: CMB anisotropies dominate at frequencies $\nu < 200$ GHz (and over the CIB up to $\lesssim 350$ GHz), whereas Galactic dust emission is preponderant at higher frequencies. On the one hand, low–frequency templates are quite effective at subtracting the CMB component from maps at few hundreds of GHz (see, e.g. Planck Collaboration XXX 2014, for a detailed discussion about this point). On the other hand, distinguishing Galactic from extragalactic dust emission is more difficult because of their fairly similar spectral energy distribution (SED) which approximately scales in both cases like a modified blackbody law. In Fig. 5, we plot the SED for the CIB intensity compared to the Galactic dust frequency spectrum (see below for the model description), normalized to the 100–GHz CIB total intensity. The spectra are almost identical at frequencies below 300 GHz, but the CIB spectrum flattens at higher frequencies, peaking at about 1000 GHz. Therefore, the two SEDs differ most in the Far–Infrared frequencies, suggesting that observations at $\gg 500$ GHz will be crucial to separate these two components.

On large areas of the sky, Galactic dust is orders of magnitude brighter than the CIB. Furthermore, it largely dominates the CIB at multipoles $\ell \lesssim 200$ in the cleanest regions of the sky (see Figure 2). Extracting the CIB signal from Galactic contamination thus requires a very accurate component separation. Currently, typical component separation methods rely on N_{HI} maps, which furnish a tracer of the dust gas (Planck Collaboration XXX 2014; Planck Collaboration XVIII 2014). However, this method has only been applied successfully over limited areas of the sky, leaving always Galactic dust residuals at the level of 5–10%. These residuals strongly affects angular scales $\ell < 200$. Component separation methods that exploit not only the frequency spectral information but also the spatial information are now being developed, with the aim to separate the two components over large areas of the sky in the *Planck* data (Planck Collaboration XLVIII 2016).

4.1 Model of the Galactic thermal dust emission

Based on the latest *Planck* results (Planck Collaboration X 2015), the frequency spectrum of the Galactic thermal dust can be accurately described by a modified blackbody

$$\Theta_d(\nu) = \left(\frac{\nu}{\nu_0}\right)^{\beta_d+3} \frac{\exp(\gamma\nu_0) - 1}{\exp(\gamma\nu) - 1}, \quad (34)$$

where ν_0 is the reference frequency (we choose $\nu_0 = 353$ GHz, if not otherwise specified) and $\gamma = 2\pi\hbar/k_B T_d$. The emissivity index β_d and the dust temperature T_d can vary on a pixel-by-pixel basis depending on the dust population and environment. We fix them to the mean values found by *Planck* (Planck Collaboration XXII 2015; Planck Collaboration X 2015), $\beta_d = 1.53$ and $T_d = 19.6$ K.

The intensity of the dust emission strongly depends on the area of the sky considered, with high–latitude regions being noticeably less affected by dust contamination. In

² <http://conservancy.umn.edu/handle/11299/169642>

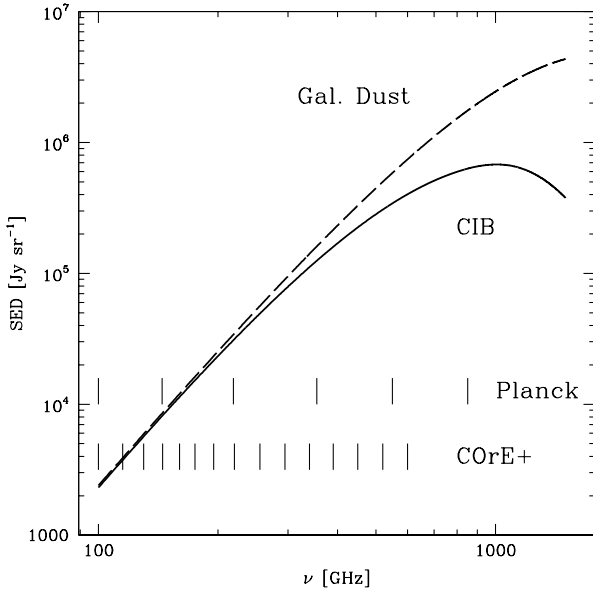


Figure 5. Frequency spectrum of the CIB brightness (solid line) and of the Galactic dust emission (dashed line) according to the models used in the paper. Dust spectrum is normalized to the CIB brightness at 100 GHz. The observational frequencies of *Planck* and CORe+ are also shown.

[Planck Collaboration XXII \(2015\)](#), the dust angular power spectrum at 353 GHz has been measured at low multipoles, $\ell < 100$, as a function of the Galactic mask (with f_{sky} varying from 40 to 80 per cent). The resulting power spectrum is well fitted by a power law with a slope consistent with -2.4 over all the Galactic masks. However, the amplitude varies nonlinearly as a function of f_{sky} . Following their Eq. (D.3), for f_{sky} between 0.4 and 0.8, we model the 353-GHz dust power spectrum (in unit of $\text{Jy}^2 \text{sr}^{-1}$) as

$$C_{\ell}^d(353) = A_d \left(\frac{\ell}{100} \right)^{\alpha_d}$$

$$A_d(f_{\text{sky}}) = 1.45 \times 10^6 \left(\frac{f_{\text{sky}}}{0.6} \right)^{[4.60+7.11\ln(f_{\text{sky}}/0.6)]}, \quad (35)$$

with $\alpha_d = -2.4$. The amplitude of the spectrum decreases therefore by a factor ~ 7 from $f_{\text{sky}} = 0.8$ to 0.6, and by a factor 2 from 0.6 to 0.4 (see Table 3).

Moving to smaller areas of the sky, we can get an estimate of the amplitude of dust power spectra from the empirical relation $C_{\ell}^d(\nu) \propto \langle I_{\nu} \rangle^2$, where $\langle I_{\nu} \rangle$ is the average dust intensity in the sky region considered. This relation, which is somewhat expected, has been tested with data at different frequencies ([Miville-Deschênes et al. 2007](#); [Planck Collaboration XXX 2016](#)). [Planck Collaboration XXX \(2016\)](#) estimated $\langle I_{\nu} \rangle$ over large regions of the sky with f_{sky} from 0.24 to 0.72, and over 352 patches of 400 deg^2 ($f_{\text{sky}} \simeq 0.01$) at Galactic latitude $|b| > 35^\circ$. The dust mean intensity was found to lower from 0.167 to $0.106 \text{ MJy sr}^{-1}$ as f_{sky} varies from 0.63 to 0.42. Based on the previous scaling relation, this translates into a decrease in the power spectrum amplitude of a factor 2.5, very close to the value given by Eq. (35) (i.e., 2.65). In the region with $f_{\text{sky}} = 0.24$, the measured mean intensity is $0.068 \text{ MJy sr}^{-1}$. This value is only about a

Table 3. Estimated amplitude of the dust angular power spectrum at 353 GHz as a function of the fraction of the sky.

f_{sky}	0.8	0.6	0.4	0.2	0.1
$A_d/10^6 [\text{Jy}^2 \text{sr}^{-1}]$	9.78	1.45	0.72	0.29	0.12

factor 1.5–2 higher than the mean intensity in the cleanest 400 deg^2 patches ($0.04\text{--}0.045 \text{ MJy sr}^{-1}$). Using the measured $\langle I_{\nu} \rangle$, we estimate A_d for $f_{\text{sky}} < 0.4$, as reported in Table 3. In particular, the value of A_d for $f_{\text{sky}} = 0.1$ has been obtained assuming a sky fraction of 10% and a dust contamination as low as the cleanest 400 deg^2 patches observed by *Planck*. This is an indicative, albeit maybe optimistic, estimate.

It is convenient to factor the auto- and cross- dust power spectra into a spatial term (Eq. 35), a frequency-dependence term (Eq. 34), and a frequency-correlation term:

$$C_{\ell}^d(\nu, \nu') = C_{\ell}^d(\nu_0) \Theta_d(\nu) \Theta_d(\nu') R_{\nu\nu'}. \quad (36)$$

The correlation between different frequency channels is then encoded in the matrix \mathbf{R} , which is assumed to be independent of the angular scales ℓ . If the signal is uncorrelated, \mathbf{R} reduces to the identity matrix (e.g., uncorrelated detector noises) while, for perfectly correlated signals, it is a rank-1 matrix containing only unit entries (e.g., CMB fluctuations). We expect that Galactic foregrounds typically fall into an intermediate case. Since we presently lack detailed measurements of the foreground correlation matrices \mathbf{R} , we decided to follow the simple model developed by [Tegmark \(1998\)](#); [Tegmark et al. \(2000\)](#) and write the correlation matrix in terms of a parameter ζ , the *frequency coherence*:

$$\mathbf{R}_{\nu\nu'} \simeq \exp \left\{ -\frac{1}{2} \left[\frac{\ln(\nu/\nu')}{\zeta} \right]^2 \right\}. \quad (37)$$

The frequency coherence determines the extent to which two frequencies can be separated before their correlation starts to break down. The two limits $\zeta \rightarrow 0$ and $\zeta \rightarrow \infty$ correspond to the two extreme cases discussed above. For foregrounds with a spectrum such as the dust emission, [Tegmark \(1998\)](#) showed that the frequency coherence is of the order of the inverse spectral index dispersion, $\zeta \approx 1/\sqrt{2}\Delta\beta$, where $\Delta\beta$ is the rms dispersion of the dust emissivity index. [Planck Collaboration XXII \(2015\)](#) measured the mean value of β at intermediate latitudes for frequencies $\leq 353 \text{ GHz}$ and found $\langle \beta \rangle = 1.51$ with $1\text{-}\sigma$ dispersion of 0.07. We shall hereafter use this value for $\Delta\beta$, which leads to a frequency coherence of $\zeta = 10.1$. In the frequency range we are interested in, this guarantees a very high level of correlation, always larger than 99%. We will investigate in §5 the effects of having larger values of $\Delta\beta$.

4.2 Dust foreground removal

Contamination by Galactic dust emission is the strongest limitation for measurements of CIB fluctuations, and accurate methods to separate it from the CIB signal are required. In this section however, we are not interested in the ability of a particular foreground subtraction method to separate dust from CIB. Instead, we shall hereafter assume that the Galactic dust removal can be done correctly down to a given

level (e.g., 10%, 1%, etc.), so that we can investigate in which way the presence of foreground residuals propagate into the uncertainty on the f_{NL} parameter.

The problem is equivalent to forecasting the detectability of the CMB B-mode polarization and the tensor-to-scalar ratio r parameter in CMB experiments (see, e.g., [Errard et al. 2016](#)). Analogously to the CMB, CIB fluctuations can be treated as being statistically isotropic on the sky, yet with the important difference that the CIB frequency spectrum is not perfectly known and depends on the CIB model parameters.

Different authors (e.g., [Tucci et al. 2005](#); [Stivoli et al. 2010](#); [Errard et al. 2016](#)) have shown that, after the subtraction, power spectra of foreground contaminants leftover in CMB maps can be fairly well described by the original power spectra scaled down by a factor that depends on details of the component separation and properties of signals. Moreover, the noise variance in the reconstructed CMB maps will be degraded according to the frequency spectrum of foregrounds and the noise in the channels involved in the foreground subtraction. Assuming that the frequency dependence of the foregrounds is perfectly known, the noise variance in the reconstructed CMB maps – obtained by a standard minimum-variance solution – is (see, e.g., [Tegmark et al. 2000](#); [Stompor et al. 2009](#); [Errard et al. 2016](#)):

$$\Sigma_{\text{CMB}}^2 = \left[(\mathbf{A}^T \mathbf{N}^{-1} \mathbf{A})^{-1} \right]_{\text{CMB CMB}}, \quad (38)$$

where \mathbf{A} is the “mixing” matrix that describes the frequency dependence of the sky signal components (i.e., CMB and foregrounds), and has a dimension of $[N_\nu \times N_s]$ (N_ν is the number of frequencies and N_s the number of sky components). The square $[N_\nu \times N_\nu]$ matrix \mathbf{N} is the noise covariance matrix. Eq. (38) is a good approximation even when the spectral behavior of foregrounds is parametrized by a set of spectral parameters which need to be determined together with the sky signal (see, however, the discussion in [Stompor et al. 2009](#)).

We extend the previous formalism to the CIB, which is now the component to be recovered. For simplicity, we assume that the sky signal is composed only of Galactic dust emission and CIB fluctuations. The elements \mathbf{A}_{i1} and \mathbf{A}_{i2} of the $[N_\nu \times 2]$ mixing matrix at the frequency i are then given by Eqs. (9) and (34), where the reference frequency ν_0 now is the frequency at which we want to recover the CIB map. If the noise in the different channels is uncorrelated, the noise variance in CIB reconstructed maps is

$$\Sigma_{\text{CIB}}^2(\nu_0) = \frac{\sum_i \Theta_d^2(i)/\sigma_i^2}{\det(\mathbf{A}^T \mathbf{N}^{-1} \mathbf{A})}, \quad (39)$$

with

$$\det(\mathbf{A}^T \mathbf{N}^{-1} \mathbf{A}) = \sum_i \frac{\Theta_{\text{CIB}}^2(i)}{\sigma_i^2} \sum_i \frac{\Theta_d^2(i)}{\sigma_i^2} - \left[\sum_i \frac{\Theta_{\text{CIB}}(i)\Theta_d(i)}{\sigma_i^2} \right]^2, \quad (40)$$

and σ_i is the noise level at the i th frequency. We see that, in the regime $\Theta_{\text{CIB}} \sim \Theta_d$ expected at frequencies $\lesssim 300$ GHz (see Figure 5), the noise in the reconstructed map diverges. Frequencies much larger than 300 GHz are therefore mandatory to separate CIB fluctuations and dust emission.

Following, e.g., [Errard et al. \(2016\)](#), we assume that the mixing matrix \mathbf{A} can be directly estimated with a set of frequency maps produced by one (or more) experiment. The reconstructed CIB map (at our reference frequency ν_0) will be then obtained by linearly combining the set of frequency maps on the basis of the mixing matrix. This can be seen as a general approach, independently of the specific component separation method employed. However, unlike for the CMB, we want to recover independent CIB maps at several frequencies. If observations are available at n frequencies ($\nu \gtrsim 200$ GHz), we assume that “clean” CIB maps can be reconstructed only in $n_{\text{CIB}} \leq n/2$ frequencies, while the other $n_d = n - n_{\text{CIB}}$ channels are dedicated to the estimation of the mixing matrix and the Galactic dust template used in the subtraction. The noise variance in a recovered CIB map is then given by Eq. (39), where the mixing matrix is evaluated using the n_d “dust” channels plus the CIB channel at ν_0 .

The auto- and cross- power spectra in clean CIB maps read

$$C_\ell^{\nu_i \nu_j} = C_\ell^{(\text{CIB})}(\nu_i, \nu_j) + \varepsilon C_\ell^d(\nu_i, \nu_j) + \Sigma_{\text{CIB}}^2(\nu_i) \delta_{ij}, \quad (41)$$

where Σ_{CIB} is the noise variance obtained from Eq. (39), and ε is the fraction of the total Galactic dust power spectrum leftover in CIB maps. We use as reference value $\varepsilon = 10^{-2}$, which implies a subtraction of the dust emission at the level of 99%. This level should be the minimum goal for future space missions characterized by high sensitivity and large frequency coverage.

In the following forecasts, we will include two extra parameters in the Fisher matrix (Eq. 32): the amplitude A_d of the dust power spectrum and the spectral power-law index α_d , shown Eq. (35). $\sigma(f_{\text{NL}})$ will be also marginalized over them.

4.3 Fisher forecasts for present and future experiments

In this section we aim to provide realistic forecasts for the detection of the f_{NL} parameter including 1) the Galactic dust contamination, as discussed above, and 2) the instrumental properties of CMB space missions. We focus on *Planck*, and on possible future experiments like CORe+, LiteBIRD ([Matsumura et al. 2014](#)) and PIXIE ([Kogut et al. 2014](#)). Table 4 gives the instrumental specifications we consider for these experiments. We take into account frequencies $\nu > 200$ GHz solely.

Planck. Observations from the *Planck* mission cover a large range of frequencies, up to 857 GHz. The 545- and 857-GHz channels are crucial for the CIB/dust separation. In our analysis we suppose that the channels at 353 and 857 GHz are dedicated to provide the dust template, while CIB maps are recovered at 217 and 545 GHz. In Table 4 we report the degraded sensitivity in these channels after the subtraction of the dust contamination (see Eq. 39). In this particular case, the 217-GHz channel gains, in term of (squared) sensitivity, a factor ~ 1.5 , while the 545-GHz channel loses sensitivity by almost a factor 6.

Assuming that the dust emission has been cleaned at a level of 1%, we find that the uncertainty on f_{NL} provided by *Planck* is $\sigma(f_{\text{NL}}) \simeq 3.5$, almost independently of the value of f_{NL} . In Figure 6 we show the relative uncertainty on f_{NL} .

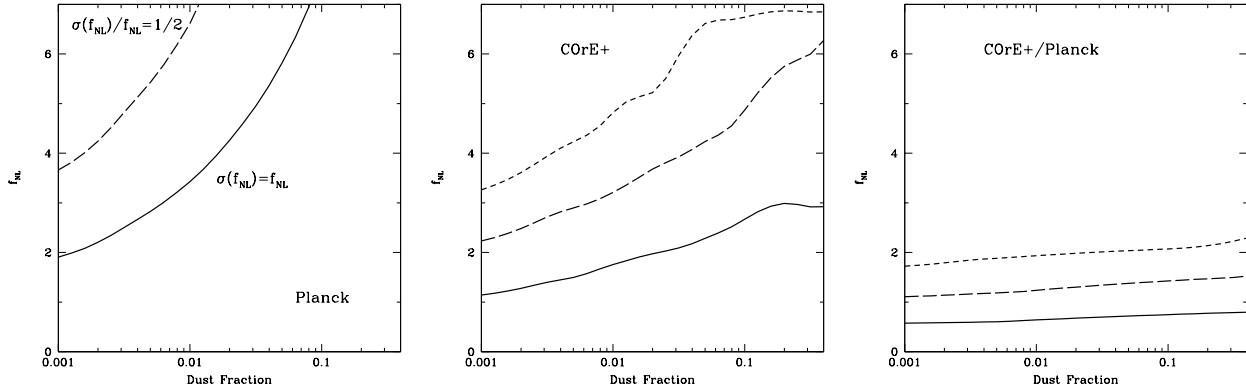


Figure 7. The value of f_{NL} for which its relative uncertainty is equal to 1 (solid lines, corresponding to a 1σ detection), $1/2$ (long dashed lines) and $1/3$ (short dashed lines) is plotted as a function of the fraction of the dust residual. This is computed for *Planck* (left panel), COre+ (middle panel) and the combination COre+/Planck (right panel), in their best configuration for CIB measurements.

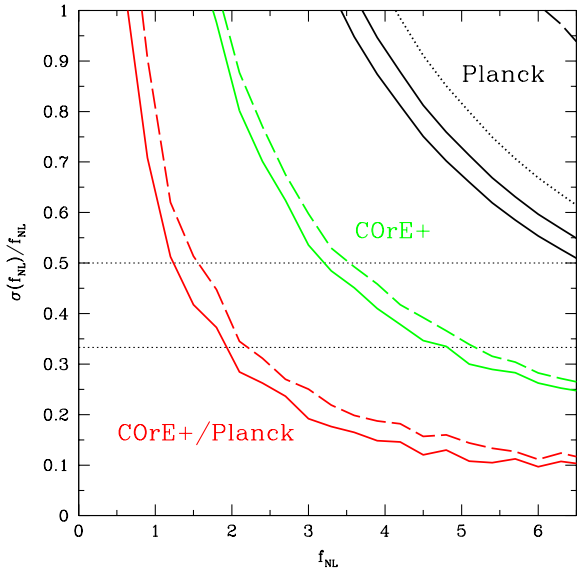


Figure 6. The relative uncertainty for positive f_{NL} obtained by Fisher forecasts for *Planck* (black lines), COre+ (green lines) and a combination of COre+ and *Planck* (red lines). The two black solid lines are for *Planck* with $f_{\text{sky}} = 0.2$ (upper) and 0.4 (lower curve; the case with $f_{\text{sky}} = 0.6$ is very close to the case with 0.4); the dotted black line is for $f_{\text{sky}} = 0.1$ and the dashed line (in the upper-right corner) for $f_{\text{sky}} = 0.8$. For COre+, the solid (dashed) green line corresponds to the configuration with 4 (3) CIB frequency maps. The red dashed line is for COre+ adding only the 857-GHz channels, and the solid line adding all the *Planck* frequencies ≥ 353 GHz (see the text and Table 4)

According to our estimates, *Planck* should be able to detect $|f_{\text{NL}}|$ at about $2\text{-}\sigma$ level if it is larger than 6, and give an upper limit of ~ 3.5 at $1\text{-}\sigma$. This would significantly improve the current constraints on the local f_{NL} provided by *Planck* using the CMB bispectrum (Planck Collaboration XVII 2015), i.e. $f_{\text{NL}} = 0.8 \pm 5.0$.

We have also considered CIB maps covering different fractions of the sky. The optimal configurations have a sky fraction $f_{\text{sky}} \simeq 0.4$, although similar results are obtained for

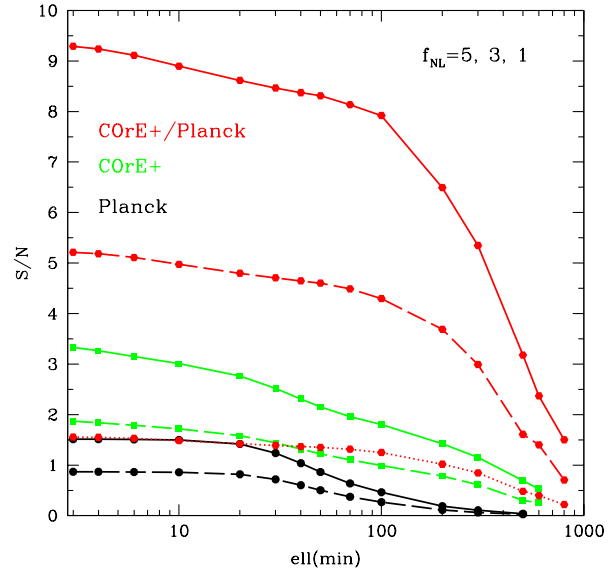


Figure 8. Signal-to-noise ratio for $f_{\text{NL}} = 5, 3$ and 1 (solid, dashed and dotted lines, respectively) as expected for *Planck* (red lines), COre+ (green lines) and the combination COre+/Planck (red lines). This is computed for $f_{\text{sky}} = 0.4$ and 1% dust residual.

$0.2 \lesssim f_{\text{sky}} \lesssim 0.6$. For smaller areas, the sensitivity to f_{NL} gets worse, while very large fractions of the sky are not useful for the f_{NL} detection due to the strong dust contamination. Finally, we show in Figure 7 the dependence of our results on the amplitude of the dust residual. The possible detection of f_{NL} strongly depends on the dust contamination. In order to improve the current *Planck* constraint on f_{NL} , dust contamination has to be removed at least at a 3% level. On the other hand, a 1 per mil cleaning would give an uncertainty of $\sigma(f_{\text{NL}}) \simeq 2$.

COre+. This project represents an approximately optimal space mission for the search of the CMB B-mode polarization, characterized by a high sensitivity of a few μK -arcmin, a few arcmin resolution and a large frequency coverage. The COre+ project is planned to include 8 frequencies

at $\nu > 200$ GHz, with the highest channel at 600 GHz. We consider two possible configurations for the measurement of the CIB: a more conservative choice involving 3 frequencies for CIB and 5 for dust, and a optimistic one with half of the frequencies reserved for each component (see Table 4). In both cases, after the component separation, the noise in the reconstructed CIB maps increases by a factor 5–10. This significant degradation in sensitivity may be related to the frequency coverage, which does not include the wavelengths at which the SEDs of the two components start to differ. As expected however, the sensitivity on f_{NL} significantly increases with respect to *Planck*, being $\sigma(f_{\text{NL}}) \gtrsim 1.6$. Consequently, $|f_{\text{NL}}| = 5$ would be measured at $\sim 3\text{-}\sigma$, and $|f_{\text{NL}}|$ of 2–3 would be also detectable with a significance of about $1\text{--}2\sigma$ (see Figure 6). The difference between the two configurations is modest, although an extra CIB frequency has been added. Here again, the best results are for sky fractions around 0.4–0.6. Looking at Figure 7, the CORe+ results appear to be less dependent on the dust residual, presumably owing to the higher instrumental sensitivity.

CORe+/Planck. The sensitivity of CORe+ to the f_{NL} parameter strongly improves when the highest *Planck* channels are also taken into account and combined with CORe+ data. Extending the frequency coverage to 857 GHz is key to better separate CIB and dust emission. It is actually enough to include the *Planck* 857–GHz channel in the mixing matrix to reduce the noise degradation in reconstructed CIB maps, at a level close to the CORe+ sensitivity (see Table 4). This is due to the different scaling of the dust and the CIB at high frequencies, see Fig. 5. In Figure 6 we show the results when *Planck* data are included to estimate the mixing matrix and the noise degradation. We see that a 3–(2–) σ detection of $|f_{\text{NL}}|$ is now possible down to values of 2 (1.5). This means that, with this configuration, the residual dust emission can be accurately separated from the CIB fluctuations. This is confirmed by the fact that reducing the level of the dust residual there is a very small improvement in the detection of f_{NL} (see Figure 7). In addition, if we increase the fraction of the sky up to $f_{\text{sky}} = 0.8$, $\sigma(f_{\text{NL}})$ always decreases.

Figure 8 shows the signal-to-noise ratio (defined as $\text{SNR} = f_{\text{NL}}/\sigma(f_{\text{NL}})$) for f_{NL} as a function of the minimum observable multipole ℓ_{min} for the three cases discussed above. It is interesting to note that for *Planck* the SNR is constant up to $\ell_{\text{min}} = 20$, indicating that at the largest angular scales the signal is completely dominated by the dust contamination. On the contrary, CORe+ succeeds to better separate the two components and to access information also at $\ell \lesssim 20$. The multipole range that contributes the most to the SNR changes according to the experiment and the configuration: in *Planck* this range is about $\ell = 20\text{--}70$; in CORe+ it extends almost up to $\ell = 300\text{--}400$; in CORe+/Planck large angular scales seem to contribute less than in the previous examples, and the SNR clearly drops only at $\ell > 100$ and the main contribution comes from scales between $\ell \sim 100$ and $\lesssim 600$.

LiteBIRD. This satellite could provide interesting constraints on f_{NL} in its extended version³, with several spectral bands spanning 40–400 GHz and 4 bands between 200 and 400 GHz. Clearly, without external information, Lite-

BIRD alone is not suitable for detecting PNG through the CIB ($\sigma(f_{\text{NL}}) \gtrsim 6$, see Table 4). However, jointly with *Planck* data, we find $\sigma(f_{\text{NL}}) \simeq 1.3$ (in a configuration where three out of four LiteBIRD channels are dedicated to the CIB), only a factor 2 larger than with CORe+.

PIXIE. The planned PIXIE mission presents almost the optimal requirements for detecting f_{NL} through CIB anisotropies, thanks to its 400 channels between 30 GHz and 6 THz and a rms sensitivity of the order of 70 nK in 1° pixels. In these conditions, dust emission should be extremely well constrained, even at the peak of the thermal emission. We expect therefore that PIXIE will be able to investigate very tiny PNG signals, with $|f_{\text{NL}}| \ll 1$. As an example, we have considered 8 frequency bands between 200 and 600 GHz with a squared sensitivity of 1 Jy sr^{-1} and a resolution of 1.6° : we obtain $\sigma(f_{\text{NL}}) \simeq 0.08$ assuming 1% of dust residual and ~ 0.07 without dust contamination. Extending the frequency range to 900 GHz (but with a similar number of frequency bands) seems not to produce any relevant improvement in the f_{NL} uncertainty. However, these results should be taken as indicative. On one hand, we expect that increasing the number of frequency bands dedicated to CIB, $\sigma(f_{\text{NL}})$ could still decrease. On the other hand, especially for the PIXIE case that can investigate very low values of f_{NL} , a more accurate analysis should be required, taking into account effects of other contaminants (CMB, extragalactic sources, etc.) and model uncertainties (e.g., in the CIB and bias prescriptions). We will discuss these issues in the next Section.

5 DISCUSSION

Model of CIB power spectra. Our Fisher forecasts rely on the fact that the CIB model we adopt provides a good description of actual CIB spectra, at least on the angular scales of interest. This is a reasonable hypothesis, considering that the model is able to fit observations for auto- and cross-frequency power spectra, number counts, and absolute CIB levels simultaneously (Viero et al. 2013; Planck Collaboration XXX 2014). However, although it successfully describes *Planck* data, it remains nonetheless a fairly simplified description of the actual CIB. Future high-quality CIB measurements (necessary to detect the f_{NL} parameter) may require an additional level of sophistication.

The CIB angular power spectra are currently well determined only at small/intermediate angular scales, i.e. $\ell \gtrsim 200$. No information is thus far available at larger scales, where the PNG effects on CIB anisotropies are most pronounced. Some concern could arise if the shape of the low- ℓ part of CIB spectra depends on model assumptions. To test this, we have compared the large-scale power spectra obtained with different CIB models, all providing a good fit to the *Planck* data. Besides the extended halo model used in this paper, we have considered: 1) a linear model where the 2-halo contribution is determined by an effective bias and by the star formation history, which in turn are constrained by *Planck* data (see §5.4 of Planck Collaboration XXX 2014); 2) a simplified halo model in which all galaxies have the same luminosity regardless of their host dark matter halo used, e.g. in Planck Collaboration XVIII (2011); Curto et al. (2015). Although they agree at $\ell \gtrsim 200$, the power spectra

³ <http://indico.cern.ch/event/506272/contributions/2138028/>

Table 4. Instrumental specifications of the space missions considered in the paper, the corresponding noise variance in the reconstructed CIB maps for different configurations (Σ^2) and the uncertainty on f_{NL} (assuming $f_{\text{NL}} = 0$).

		Planck								$\sigma(f_{\text{NL}})$
ν [GHz]	217			353			545		857	
fwhm [arcmin]	5.02			4.94			4.83		4.64	
w^{-1} [$\text{Jy}^2 \text{sr}^{-1}$]	43.32			164.7			185.3		157.9	
Σ^2 [$\text{Jy}^2 \text{sr}^{-1}$]	29.0			–			1100		–	3.6
CORe+										
ν [GHz]	220	255	295	340	390	450	520	600		
fwhm [arcmin]	3.82	3.29	2.85	2.47	2.15	1.87	1.62	1.40		
w^{-1} [$\text{Jy}^2 \text{sr}^{-1}$]	0.654	1.43	5.20	8.31	13.50	22.98	39.88	69.26		
Σ^2 [$\text{Jy}^2 \text{sr}^{-1}$]	–	8.03	–	47.3	–	–	377.	–		1.8
	–	8.04	–	47.3	–	212.	382.	–		1.6
with Planck 857 GHz	–	1.83	–	10.0	–	–	82.6	147.		0.7
with Planck	–	1.97	–	10.8	–	45.6	90.2	163.6		0.6
LiteBIRD										
ν [GHz]	235		280	337	402					
fwhm [arcmin]	30		30	30	30					
w^{-1} [$\text{Jy}^2 \text{sr}^{-1}$]	0.36		1.45	1.1	0.7					
Σ^2 [$\text{Jy}^2 \text{sr}^{-1}$]	11.3			149.5						6.4
with Planck	1.0			6.7	14.6					1.3
PIXIE										
ν [GHz]	218	248	293	353	398	443	548	593		
fwhm [arcmin]	96	96	96	96	96	96	96	96		
Σ^2 [$\text{Jy}^2 \text{sr}^{-1}$]	1.0	1.0	1.0	1.0	1.0	1.0	1.0	1.0		0.08
no dust	1.0	1.0	1.0	1.0	1.0	1.0	1.0	1.0		0.07

exhibit a different behavior at the largest scales (see left panel of Figure 9). Our reference model peaks at higher angular scales and has significantly less power at $\ell \lesssim 100$. The main factor that determines the low- ℓ behavior in the CIB spectra is the redshift evolution of the average galaxy emissivity, $\bar{j}_\nu(z)$. In fact, when the same $\bar{j}_\nu(z)$ is applied to the different CIB models, the low- ℓ power spectra become very similar, and even indistinguishable (after a proper renormalization) as shown in the right panel of Figure 9. Overall, the PNG features in the CIB power spectra seem to weakly depend on the model prescription⁴.

In order to distinguish PNG signals, it is therefore key to correctly model the evolution of the infrared galaxy emissivity. Accurate measurements of CIB power spectra at degree scales should further strengthen the model reliability, especially concerning this point. Estimates of number counts, luminosity and correlation functions of infrared galaxies at shorter wavelengths should also provide complementary information. In addition, as shown in Planck Collaboration XXX (2016), the evolution of the galaxy emissivity can be related to the star formation density history. The

linear model and the extended halo model recover consistent star formation histories below $z = 2$, in agreement with recent measurements by *Spitzer* and *Herschel*, while at higher redshifts, there are discrepancies between the two models and between models and observational estimates (see discussion in Planck Collaboration XXX 2016). In the future, we expect that a better determination of the history of the star formation density will improve significantly the constraints on the galaxy emissivity and then will help to fix the CIB spectral behavior at low ℓ s.

Moreover, we have shown in §2.3 that the relative amplitude of the non-Gaussian CIB bias could depend on the HOD parameter M_{eff} , i.e. on the range of halo masses that are most efficient at hosting star formation. In the extended halo model this parameter is assumed to be constant in time, in agreement with results from Behroozi et al. (2013), at least out to $z = 4$. However, they found a much lower value for the characteristic halo mass (i.e. $\log(M_{\text{eff}}/M_\odot) = 11.7$) compared to the Planck results. We have verified that, using this value for M_{eff} , CIB spectra change in amplitude but not in shape, even with $f_{\text{NL}} \neq 0$. This is an important indication that the PNG signal is fairly insensitive to the HOD parameters. Note, however, that we have extrapolated the subhalo mass function of Tinker & Wetzell (2010) much beyond its actual range of validity, i.e. $0.8 < z < 1.6$. Furthermore, while the amplitude non-Gaussian bias is generally given by derivative of \bar{n}_h relative to the normalisation σ_8

⁴ In Figure 9, for the linear model, we have considered only the Gaussian case. In fact, for this model it is not straightforward to introduce a NG bias due to the parametric approach used for the effective bias of infrared galaxies (see Planck Collaboration XXX 2014).

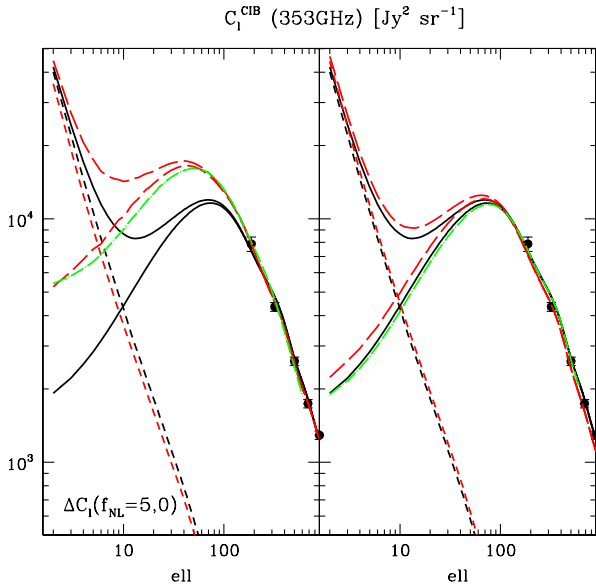


Figure 9. *Left panel* CIB power spectra with $f_{\text{NL}} = 0$ and 5, according to different model approaches: the extended halo model used in the paper (solid black lines); the simplified halo model (red long dashed lines); the linear model (green dash-dotted line, only $f_{\text{NL}} = 0$). Short dotted lines shows the difference between the Gaussian case and $f_{\text{NL}} = 5$. Points represent *Planck* measurements (Planck Collaboration XXX 2016). CIB spectra differ at $\ell < 200$. *Right panel* The same as in the left panel, but here spectra are computed using the same galaxy emissivity evolution as given by the extended halo model. Differences in CIB spectra are now small or negligible over all the multipole range considered. In either case, the PNG signal seems to be independent on the model approach.

(Slosar et al. 2008), we have assumed a universal halo mass function \bar{n}_h , which implies $\partial \ln \bar{n}_h / \partial \ln \sigma_8 = \delta_c b_1$. The validity of this assumption may, however, depend on the halo identification algorithm (Desjacques & Seljak 2010). Although N-body simulations support universality when the mass of SO halos is $M \gtrsim 10^{13} M_\odot$ (Desjacques et al. 2009), the extent to which this assumption holds at smaller masses is still a matter of debate.

Galactic dust emission. Due to its relevance, we should investigate the extent to which our results are sensitive to the Galactic dust model used in the analysis. Dust residual in CIB reconstructed maps is parametrized – see Section 4.1 and Eq. (36) – by the product of spatial, frequency and correlation terms. In particular, by taking the correlation matrix $R_{\nu\nu'}$ independent of the angular scale, we are supposing that the shape of dust residual power spectra are the same over all the frequencies. This is something expected and supported by simulations of component separation performance (Curto et al. 2016).

Two free parameters are considered for dust residual power spectra and then marginalized in the Fisher approach: the amplitude and the power-law index of the power spectrum at the reference frequency. The dust SED is instead assumed to be perfectly known. This is motivated by the fact that this Galactic contaminant largely dominates the sky emission at $\nu \gtrsim 300$ GHz, especially on large angular scales, and the frequency spectrum is expected to be accurately de-

Table 5. Frequency coherence of the dust emission and the uncertainty on the f_{NL} parameters as a function of the spatial dispersion of the dust spectral index.

$\Delta\beta$	0.07	0.1	0.3	0.5
ν/ν'	$R_{\nu\nu'}$			
1.5	> 0.99	> 0.99	0.985	0.96
2	> 0.99	> 0.99	0.96	0.89
3	> 0.99	0.99	0.90	0.74
4	0.99	0.98	0.84	0.62
	$\sigma(f_{\text{NL}})$			
<i>Planck</i>	3.6	4.2	7.5	9.1
<i>COreE+</i>	1.6	1.9	2.9	3.3
<i>COreE+/Planck</i>	0.6	0.64	0.72	0.76

termined across the sky. This hypothesis can be relaxed by adding as extra free parameter the dust emissivity index β_d . We have verified however that it has a negligible impact on the f_{NL} uncertainty.

A more critical issue in the Fisher analysis is the frequency coherence in the dust residual. We have related it to the spatial dispersion of the dust emissivity index, according to the prescription proposed by Tegmark (1998). Planck Collaboration XXII (2015) found that the variance across the sky of the dust spectral index is $\Delta\beta \simeq 0.07$ which corresponds to a frequency correlation level larger than 99% (between 200 and 900 GHz). It is clear that reducing the frequency coherence of the dust emission can significantly degrade the sensitivity on the f_{NL} parameter for experiments covering a large frequency range. In Table 5 we compute the frequency coherence values as increasing $\Delta\beta$. We can see that dust emission is still highly correlated for $\Delta\beta \simeq 0.1$, even between well separated frequencies, while some decorrelation is observed for $\Delta\beta \sim 0.3$ and $\nu/\nu' > 2$. The uncertainty on f_{NL} from *Planck* or *COreE+* seems to be quite sensitive to the frequency coherence and increases by $\sim 20\%$ if $\Delta\beta = 0.1$. On the contrary, when *Planck* and *COreE+* are combined, the frequency decorrelation has little impact on results.

Dust contamination and Fisher forecasts. As an alternative approach to estimate f_{NL} constraints in the presence of dust contamination, we compute the Fisher matrix without assuming any foreground removal. We include in the analysis all the observational frequencies for a given experiment at their nominal sensitivity. We expect this approach to produce more conservative results. Dust removal on maps should be in fact more powerful and effective than a CIB–dust emission separation at the level of power spectra. It is also an useful test to check if our working hypothesis (e.g., dust removal at a 1 per cent level in about half of the observational frequencies) are too conservative or too optimistic. For *Planck* we find $\sigma(f_{\text{NL}}) \simeq 5$, about a 50 per cent larger than previous results with 1% dust residual. In this case, a component separation approach to remove the dust contamination is strictly required. On the other hand, in the case of *COreE+*, if we consider all the 8 frequencies between 200 and 600 GHz at their nominal sensitivity, the uncertainty on f_{NL} significantly decreases with respect to previous values, and we find $\sigma(f_{\text{NL}}) \simeq 0.25$ (to be compared with ~ 1.6 and 0.6

for COre+ and COre+/Planck, respectively). This result is very close to the one obtained without any dust contamination in §3. Similarly, for LiteBIRD we obtain $\sigma(f_{\text{NL}}) \simeq 0.33$. Such an improvement can be explained by the very small noise level expected in future experiments (not degraded by component separation) together with a larger number of frequency channels. We therefore conclude that, in principle, the dust contamination should be fully controlled by high-sensitive observations at a sufficient number of frequencies. Previous results for COre+ and LiteBIRD mission might be then conservative, at least in terms of the number of frequencies to be exploited for the CIB.

For the purpose of computing the Fisher matrix we fixed the fiducial cosmological model. This assumption contributes to a possible theoretical systematic uncertainty. However, the Planck satellite has measured the parameters of the cosmological standard model to high precision (Planck Collaboration XIII 2015). For example, the tilt of the primordial spectrum might be partially degenerate with the CIB slope at low ℓ . But Planck has determined the value of the scalar spectral index with tiny error bars, $n_s = 0.968 \pm 0.006$. In addition, the Planck data covers a wide range of scales, and there is no indication for a running of the scalar spectral index or any other significant deviation from a power law spectrum, except maybe a (not significant) power deficit on large scales (Planck Collaboration XX 2015). The power deficit can hardly be confused with the expected excess power on the largest scales in the CIB from non-Gaussian bias if $f_{\text{NL}} > 0$, and also the curves for $f_{\text{NL}} < 0$ turn back up at the lowest ℓ so that we do not expect this to be a problem.

Finally, we did not fully take into account the non-Gaussianity of the CIB covariance matrix, although the CIB power spectrum includes the non-Gaussian bias. We have ignored the contribution induced by a primordial four-point function (or trispectrum) which, in the PNG model considered here, is proportional to f_{NL}^2 . This term might not be negligible at low multipoles. The covariance will also include contributions generated by the nonlinear gravitational evolution. They will involve, among others, the CIB bispectrum. However, these terms scale at best like k^2 in the power of biased tracers. Therefore, we expect them to contribute much less than the 1-halo term at low multipoles.

Overall, $\sigma(f_{\text{NL}}) < 1$ results should be taken with some caution. For example, according to our estimates, PIXIE has the potentiality to detect PNG signals from $f_{\text{NL}} < 0.1$. However, as discussed in this section, our Fisher forecasts are based on some theoretical assumptions (e.g., the bias prescription, Gaussian covariance matrix, etc.), and on a particular CIB modeling framework, whose validity and impact on results has not been fully investigated. Finally, possible systematics in future data and extra astrophysical contaminants (as CMB, point sources, thermal Sunyaev–Zeldovich effect) have not been considered in the present analysis. All these aspects should be investigated in future works.

6 CONCLUSION

In this paper we investigate the ability of CIB observations at frequencies of a few hundred GHz (i.e. where CMB exper-

iments operate) to detect local primordial non-Gaussianity, and measure the nonlinear parameter f_{NL} by leveraging the scale dependent bias on large scales.

We model the CIB angular power spectrum under the assumption that the cosmic infrared background is produced by star-forming galaxies emitting at infrared wavelengths. We describe the clustering of these galaxies using a halo model, with a galaxy luminosity–halo mass relation as adopted in Shang et al. (2012); Planck Collaboration XXX (2014). We take into account both general relativistic corrections and the scale-dependent non-Gaussian halo bias induced by the local primordial non-Gaussianity. We perform a Fisher forecast to ascertain the precision at which f_{NL} can be measured by CMB space missions.

We find that the GR corrections are subdominant except at the largest angular scales. The leading contribution arises from the Doppler term, although it only makes up less than 50% of the CIB angular power spectrum at 353 GHz for $\ell = 2$ (where cosmic variance is largest), higher frequencies. At $\ell = 10$, the GR corrections are reduced to the percent level, corresponding to a local bispectrum shape with amplitude $f_{\text{NL}} \simeq 0.1$.

Under the ideal condition of perfect dust subtraction over 40% of the sky, future CMB space missions like COre+, operating at frequencies between 200 and 600 GHz, shall be able to detect $f_{\text{NL}} \sim 1$ with high significance ($> 2\sigma$), when several frequencies are combined. In this case, information from the very large angular scales, i.e. the ones most affected by Galactic dust, is not strictly required.

Of course, a complete subtraction of dust is unlikely. Therefore, we have also produced forecasts assuming a dust subtraction at the 1% level in the best scenario. In this case, an experiment with a Planck-like sensitivity should be able to reach an uncertainty on f_{NL} of $\sigma(f_{\text{NL}}) \sim 3.5$ for sky fractions between 0.2 and 0.6. Larger sky fractions are not useful because of the strong dust contamination, which actually degrades the constraints. Future probes like COre+, LiteBIRD and PIXIE, which have a higher sensitivity and more frequency channels, should be able to constrain f_{NL} to much lower values, even in a situation where the lowest multipoles could not be used owing to foreground contamination, systematic effects, or a residual dust fraction higher than expected after the cleaning. We have found that the presence of high-frequency channels in the range of 800 to 1000 GHz is especially important to reduce the impact of dust and reach $|f_{\text{NL}}| < 1$. Future missions should thus either include detectors at those frequencies or, alternatively, combine their data with the Planck 857 GHz to achieve this precision.

To conclude, an analysis of current CIB observations should in principle already yield bounds on the local f_{NL} competitive with those obtained from the analysis of non-Gaussianity in the Planck CMB maps. The CIB holds the promise of reaching $|f_{\text{NL}}| \lesssim 1$ in a not so distant future. Although not considered here, additional information could also be harvested from a cross-correlation of the “CMB lensing potential” and CIB anisotropies. This is expected to be less sensitive to the PNG but, at the same time, less affected by dust contamination (Anthony Challinor, private communication). While direct observations of the large scale structure might eventually prove even more sensitive, the CIB will remain an invaluable tool to cross-check detections or

limits from LSS due to the different systematics present in these various probes.

ACKNOWLEDGMENTS

It is a pleasure to thank Camille Bonvin and Anthony Challinor for helpful discussions. MT is also thankful to Enrique Martínez–González and Patricio Vielva for useful discussions about Fisher matrix forecasts. VD and MK are grateful to the Galileo Galilei Institute and the organizers of the workshop on “Theoretical Cosmology in the Era of Large Surveys”, during which part of this work was completed. The authors acknowledge support by the Swiss National Science Foundation. Part of the analysis was performed on the BAOBAB cluster at the University of Geneva.

APPENDIX A: GENERAL RELATIVISTIC CORRECTIONS TO THE CIB INTENSITY

We provide details about the calculation of the GR correction to the CIB brightness. We refer the reader to the intensity mapping studies of [Hall et al. \(2013\)](#); [Alonso et al. \(2015\)](#) for complementary information.

A1 CIB brightness

Let $I(\nu_o)$ be the observed CIB brightness (in units of Jy sr^{-1}), i.e. the amount of energy dE_o that passes through a proper surface element dA_o (transverse to the observed ray direction) per frequency interval $d\nu_o$, per proper time $d\tau_o$ and per solid angle $d\Omega_o$,

$$I(\nu_o) = \frac{dE_o}{d\tau_o d\nu_o d\Omega_o dA_o}. \quad (\text{A1})$$

The corresponding number of photons received by the observer is $dN_o = dE_o/h\nu_o$. Conservation of photon number (which follows from Liouville’s phase space conservation law) implies $dN_o = dN_s$, where dN_s is the infinitesimal number of photons emitted by the source. Namely,

$$\begin{aligned} I(\nu_o) &= \frac{\nu_o}{\nu_s} \frac{dE_s}{d\tau_s d\nu_s d\Omega_s dA_s} \frac{d\tau_s d\nu_s}{d\tau_o d\nu_o} \frac{d\Omega_s dA_s}{d\Omega_o dA_o} \\ &= (1+z)^{-3} \frac{dE_s}{d\tau_s d\nu_s d\Omega_s dA_s}. \end{aligned} \quad (\text{A2})$$

To derive the second equality, we have used $\nu_o/\nu_s = d\tau_s/d\tau_o = (1+z)^{-1}$ and the reciprocity relation $D_L = (1+z)D_A$, where $D_A = \sqrt{dA_s/d\Omega_o}$ and $D_L = \sqrt{dA_o/d\Omega_s}$ are the angular diameter distance and (redshift-corrected) luminosity distance, respectively. Note that the luminosity and angular distances have canceled each other out of the last expression.

Let λ be the affine parameter of the light ray $x^\mu(\lambda)$, so that $k^\mu = dx^\mu/d\lambda$ is its wavevector. During an interval $d\lambda$, the wavefront seeps out a proper volume $dV_s = dl_s dA_s$, where $dl_s = k_\mu u_s^\mu d\lambda$ is proportional to the 4-velocity u_s^μ of the emitter. Therefore, the above relation becomes

$$\begin{aligned} I(\nu_o) &= (1+z)^{-3} \frac{dE_s}{d\tau_s d\nu_s d\Omega_s dV_s} (k_\mu u_s^\mu) d\lambda \\ &= (1+z)^{-3} J_{\nu_s}^{\text{phys}} (k_\mu u_s^\mu) d\lambda, \end{aligned} \quad (\text{A3})$$

where

$$J_{\nu_s}^{\text{phys}} = \frac{dE_s}{d\tau_s d\nu_s d\Omega_s dV_s} \quad (\text{A4})$$

is the source emissivity per *physical* volume (in unit of $\text{Jy sr}^{-1} \text{m}^{-3}$). In the case of a continuous medium, Eq. (A3) must be integrated along the light ray. Hence, we can write

$$I(\nu_o, \hat{n}) = \int d\lambda (k_\mu u_s^\mu) \frac{J_{(1+z)\nu_o}^{\text{phys}}(\lambda)}{(1+z)^3}, \quad (\text{A5})$$

where \hat{n} is the observed angular position. In principle, we should also take into account the loss of intensity as the photons propagate through the intergalactic medium and modify the above relation accordingly:

$$I(\nu_o, \hat{n}) = \int d\lambda (k_\mu u_s^\mu) \frac{J_{(1+z)\nu_o}^{\text{phys}}(\lambda)}{(1+z)^3} e^{-\tau(\nu_o, \hat{n}, \lambda)}, \quad (\text{A6})$$

where $\tau(\nu_o, \hat{n}, \lambda)$ is the optical depth along the path of the ray. For simplicity however, we will ignore the beam absorption in what follows, as the focus is the evaluation of Eq. (A5) at linear order in metric perturbations.

A2 GR corrections at first order in perturbations

We consider a perturbed FRW metric in the conformal Newtonian gauge with coordinates $x^\mu = (\eta, x^i)$,

$$ds^2 = a^2(\eta)(\eta_{\mu\nu} + h_{\mu\nu})dx^\mu dx^\nu, \quad (\text{A7})$$

where

$$h_{00} = -2\Psi, \quad h_{0i} = 0, \quad h_{ij} = -2\Phi\delta_{ij}. \quad (\text{A8})$$

The perturbed photon wavevector $k^\mu = dx^\mu/d\lambda$ corresponding to the light ray $x^\mu(\lambda)$ can be written as

$$k^\mu = \frac{1}{a^2}(-1 + \delta\nu, \hat{n} + \delta\hat{n}), \quad (\text{A9})$$

where $\delta\nu$ is the fractional frequency perturbation and $\delta\hat{n}$ is the change in the propagation direction, which is such that $\hat{n}^2 = 1$ and $\hat{n} \cdot \delta\hat{n} = 0$. Since lightlike geodesics are conformally invariant, the metric $(\eta_{\mu\nu} + h_{\mu\nu})dx^\mu dx^\nu$ admits the same photon geodesics which we parametrize as $x^\mu(\tilde{\lambda})$. The corresponding photon wavevector $\tilde{k}^\mu = dx^\mu/d\tilde{\lambda}$ is related to k^μ through

$$\tilde{k}^\mu = a^2 k^\mu. \quad (\text{A10})$$

Hence, the two affine parameters satisfy $\lambda = a^2 \tilde{\lambda}$ up to an irrelevant constant.

We calculate the change in the perturbed photon wavevector \tilde{k}^μ using the geodesic equation

$$\frac{d}{d\tilde{\lambda}} \tilde{k}^\mu = -\Gamma_{\alpha\beta}^\mu \tilde{k}^\alpha \tilde{k}^\beta, \quad (\text{A11})$$

where $\Gamma_{\nu\lambda}^\mu$ are the Christoffel symbols in the conformally transformed metric. At linear order in perturbations, only the first geodesic equation describing the frequency shift is relevant as lensing of the uniform CIB yields the same CIB. Nonetheless, lensing magnification induces a first order perturbation to the CIB brightness through the flux limiting value. We will discuss this effect below. The relevant Christoffel symbols are $\Gamma_{00}^0 = \dot{\Psi}$, $\Gamma_{0i}^0 = \Psi_{,i}$ and $\Gamma_{ij}^0 = -\dot{\Phi}\delta_{ij}$,

where \dot{X} and $X_{,i}$ designate a derivative w.r.t. η and x^i , respectively. Linearizing the first geodesic equation, we arrive at

$$\frac{d}{d\lambda}\delta\nu = 2\frac{d\Psi}{d\lambda} + \dot{\Psi} + \dot{\Phi} \quad (\text{A12})$$

upon taking advantage of the fact that the derivative w.r.t. $\tilde{\lambda}$ is

$$\frac{d}{d\tilde{\lambda}} \equiv \tilde{k}^\mu \partial_\mu \approx -\partial_\eta + \tilde{n}^i \partial_i \quad (\text{A13})$$

at first order in perturbations. Eq. (A12) easily integrates to

$$\delta\nu(\lambda) - \delta\nu_o = 2(\Psi(\lambda) - \Psi_o) + \int_0^\lambda d\lambda' (\dot{\Psi} + \dot{\Phi}). \quad (\text{A14})$$

It is now expressed in terms of the affine parameter λ , which we assume to be $\lambda = 0$ at the observer position. Furthermore, $\Psi_o = \Psi(\lambda = 0)$, $\delta\nu_o = \delta\nu(\lambda = 0)$ etc.

Assuming that the source at affine parameter λ (a galaxy contributing to the CIB) and the observer move with a 4-velocity $u^\mu = a^{-1}(1 - \Psi, v^i)$ and $u_o^\mu = a_o^{-1}(1 - \Psi_o, v_o^i)$, where v_i is the proper peculiar velocity, the redshift of the emitter relative to the observer (which could be measured if e.g. emission lines were resolved) is

$$1 + z(\lambda) = \frac{(a^{-2}u_\mu \tilde{k}^\mu)_\lambda}{(a^{-2}u_\mu \tilde{k}^\mu)_o} \equiv \frac{1 + \delta z(\lambda)}{a(\eta(\lambda))}, \quad (\text{A15})$$

where $1/a(\eta(\lambda))$ is the source redshift in an unperturbed universe, and

$$\delta z(\lambda) = -(\Psi - \Psi_o) - \int_0^\lambda d\lambda' (\dot{\Psi} + \dot{\Phi}) + (\mathbf{v} - \mathbf{v}_o) \cdot \hat{\mathbf{n}} \quad (\text{A16})$$

is the redshift perturbation. Note that the boundary terms at the observer position generate an unmeasurable monopole ($-\Psi_o$) and a dipole ($\mathbf{v}_o \cdot \hat{\mathbf{n}}$), which we will ignore in what follows.

Since the emissivity j_ν^{phys} explicitly depends on the observed redshift through $\nu = (1+z)\nu_o$, it is convenient to re-parametrize the light ray as a function of z , so that

$$I(\nu_o; \hat{\mathbf{n}}) = \int dz \left(k_\mu u^\mu \frac{d\lambda}{dz} \right) \frac{j_{(1+z)\nu_o}^{\text{phys}}(z, \mathbf{x}(z))}{(1+z)^3}. \quad (\text{A17})$$

Therefore, fluctuations are now defined at the hypersurfaces of constant observed redshift z . We begin by evaluating the term $k_\mu u^\mu (d\lambda/dz)$. Using $k_\mu u^\mu = a^{-1}(\eta)(1+z)$ with $z(\lambda)$ given by Eq. (A15), we obtain

$$k_\mu u^\mu \frac{d\lambda}{dz} = \frac{a^2(\eta(z))}{\mathcal{H}(\eta(z))} \left(1 + \delta\nu - \frac{a^2(\eta(z))}{\mathcal{H}(\eta(z))} \frac{d\delta z}{d\lambda} \right). \quad (\text{A18})$$

We must now take into account the fact that the coordinate time fluctuates at fixed observed redshift z . Writing $\eta(z) = \bar{\eta}(z) + \delta\eta$, where $\bar{\eta}$ is the conformal time corresponding to the observed redshift z in the unperturbed background, the perturbation to a^2/\mathcal{H} reads

$$\frac{a^2(\eta)}{\mathcal{H}(\eta)} = \frac{a^2(z)}{\mathcal{H}(z)} \left[1 + \left(2\mathcal{H} - \frac{\dot{\mathcal{H}}}{\mathcal{H}} \right) \delta\eta \right], \quad (\text{A19})$$

where $a(z) \equiv a(\bar{\eta}(z))$, $\mathcal{H}(z) \equiv \mathcal{H}(\bar{\eta}(z))$ and the overdot designates a derivative w.r.t. $\bar{\eta}$. The time perturbation $\delta\eta$ can be read off from Eqs. (A15) and (A16) as

$$\mathcal{H}\delta\eta = -\Psi - \int_0^{\lambda(z)} d\lambda' (\dot{\Psi} + \dot{\Phi}) + \mathbf{v} \cdot \hat{\mathbf{n}}. \quad (\text{A20})$$

Here, $\lambda(z)$ is the value of the affine parameter at the observed redshift z . Therefore, with the help of the relation $\mathcal{H}\delta\eta + \delta\nu = \Psi + \mathbf{v} \cdot \hat{\mathbf{n}}$, we eventually arrive at

$$k_\mu u^\mu \frac{d\lambda}{dz} = \frac{a^2(z)}{\mathcal{H}(z)} (1 + \delta_{\parallel}) \quad (\text{A21})$$

where

$$\delta_{\parallel} = -\left(\frac{\dot{\mathcal{H}}}{\mathcal{H}} - \mathcal{H} \right) \delta\eta + \Psi + \mathbf{v} \cdot \hat{\mathbf{n}} + \frac{a^2(z)}{\mathcal{H}(z)} \left[\frac{d\Psi}{d\lambda} + (\dot{\Psi} + \dot{\Phi}) - \frac{d\mathbf{v}}{d\lambda} \cdot \hat{\mathbf{n}} \right] \quad (\text{A22})$$

is the fractional change in dl_s , i.e. in the source volume element along the line of sight. Note that the second term in the square brackets can be evaluated using $(d/d\tilde{\lambda}) = a^2(d/d\lambda)$.

We now turn to the emissivity j_ν^{phys} . With the time slicing adopted here, perturbations to the emissivity are defined at constant observed redshift z :

$$a^3 j_\nu^{\text{phys}}(z, \mathbf{x}) = a^3(z) \bar{j}_\nu^{\text{phys}}(z) (1 + \delta_j^z(z, \mathbf{x})), \quad (\text{A23})$$

where it is understood that all quantities are evaluated at a frequency $\nu = (1+z)\nu_o$. In practice, it is useful to relate the (gauge-invariant) fluctuation δ_j^z to the perturbation δ_j^N in the conformal Newtonian gauge adopted for this calculation. δ_j^N is defined on slices of constant coordinate time η , whence

$$a^3(z) \bar{j}_\nu^{\text{phys}}(z) (1 + \delta_j^z(z, \mathbf{x})) = a^3(\eta) \bar{j}_\nu^{\text{phys}}(\eta) (1 + \delta_j^N(\eta, \mathbf{x})) \quad (\text{A24})$$

Since, at fixed observed redshift, $\eta(z) = \bar{\eta}(z) + \delta\eta$ where $\delta\eta$ is given by Eq. (A20), we find after some algebra

$$\delta_j^z = \delta_j^N + \left(\frac{\dot{\bar{j}}_\nu^{\text{phys}}}{\bar{j}_\nu^{\text{phys}}} + 3\mathcal{H} \right) \delta\eta = \delta_j^N + \frac{\dot{\bar{j}}_\nu}{\bar{j}_\nu} \delta\eta \quad (\text{A25})$$

at first order in perturbations. Here and henceforth, $j_\nu = a^3 j_\nu^{\text{phys}}$ is the *comoving* emissivity. Taking into account the factor $(1+z)^{-3} \equiv a^3(z)$ in Eq. (A17), the CIB brightness simplifies to

$$I(\nu_o; \hat{\mathbf{n}}) = \int dz \frac{a^2(z)}{\mathcal{H}(z)} \bar{j}_\nu(z) \left(1 + \delta_j^N + \frac{\partial \ln \bar{j}_\nu}{\partial \bar{\eta}} \delta\eta + \delta_{\parallel} \right), \quad (\text{A26})$$

with $\nu = (1+z)\nu_o$.

Lastly, we must also take into account the fact that the CIB is produced by sources below a certain flux limiting value S_ν^{cut} . Owing to fluctuations in the luminosity distance, this corresponds to a maximum luminosity $L_\nu^{\text{cut}}(z, \hat{\mathbf{n}})$ which depends on redshift and position on the sky. At first order in perturbations, we get

$$L_\nu^{\text{cut}}(z, \hat{\mathbf{n}}) = \bar{L}_\nu^{\text{cut}}(z) (1 + 2\delta_{\perp}). \quad (\text{A27})$$

The threshold luminosity $\bar{L}_{\text{cut}}(z)$ is related to the flux detection limit S_{cut} through

$$\bar{L}_\nu^{\text{cut}}(z) = 4\pi(1+z)^4 a^2(z) \bar{\chi}^2(z) S_\nu^{\text{cut}}, \quad (\text{A28})$$

where $\bar{\chi}(z)$ is the line-of-sight comoving distance corresponding to the redshift z in the unperturbed background. The perturbation δ_{\perp} transverse to the photon propagation at the source position is given by Eq. (19). Therefore, the average CIB emissivity \bar{j}_ν per comoving volume in Eq. (A26)

should be replaced by

$$\int_0^{\bar{L}_\nu^{\text{cut}}(z, \hat{n})} dL \bar{n}_g(L, z) \frac{L^{(1+z)\nu}}{4\pi} \\ = \bar{j}_\nu(z) + 2 \bar{n}_g(\bar{L}_\nu^{\text{cut}}(z)) \frac{\bar{L}_\nu^{\text{cut}}(z)}{4\pi} \delta_\perp,$$

where, in $\bar{j}_\nu(z)$, the integral over galaxy luminosities runs from 0 to $\bar{L}_\nu^{\text{cut}}(z)$. The perturbed CIB comoving emissivity at hypersurfaces of constant observed redshift thus reads

$$j_\nu(z, \mathbf{x}) = \bar{j}_\nu(z) \left(1 + \delta_j^N + \frac{\partial \ln \bar{j}_\nu}{\partial \eta} \delta \eta + \delta_\parallel + 2 \frac{\bar{n}_g}{\bar{j}_\nu} \frac{\bar{L}_\nu^{\text{cut}}}{4\pi} \delta_\perp \right) \quad (\text{A29})$$

for a given flux detection limit S_ν^{cut} .

Finally, all the background quantities are thus far been evaluated at $\bar{\eta}(z)$. However, since the unperturbed photon path can also be parametrized as $x^\mu(\bar{\chi}) = (\eta_0 - \bar{\chi}, \bar{\chi})$, we can recast the CIB brightness into Eq. (15) with the aid of $d\bar{\chi}/dz = a(\bar{\eta}(z))/\mathcal{H}(\bar{\eta}(z))$.

A3 Imprint on the CIB angular power spectrum

Fluctuations in the CIB intensity can be expanded in the basis of spherical harmonics Y_ℓ^m as

$$I(\nu, \hat{\mathbf{n}}) = \sum_{\ell m} a_{\ell m}(\nu) Y_\ell^m(\hat{\mathbf{n}}). \quad (\text{A30})$$

The frequency-dependent multipoles $a_{\ell m}(\nu)$ are given by the line-of-sight integral

$$a_{\ell m}(\nu) = \int dz \left(\frac{d\chi}{dz} \right) a(z) \bar{j}_\nu(z) \Delta_{\ell m}(\nu, z), \quad (\text{A31})$$

where χ now is the unperturbed line-of-sight comoving distance (we drop hereafter the overline for shorthand convenience), and

$$\Delta_{\ell m}(\nu, z) = \int d\hat{\mathbf{n}} Y_\ell^{m*}(\hat{\mathbf{n}}) \left(\delta_j^N + \frac{\dot{j}_\nu}{\bar{j}_\nu} \delta \eta + \delta_\parallel + 2 \frac{\bar{n}_g}{\bar{j}_\nu} \frac{\bar{L}_{\text{cut}}}{4\pi} \delta_\perp \right) \\ = \sum_S \Delta_{\ell m}^S(\nu, z) \quad (\text{A32})$$

has been schematically decomposed in §2.2 into a sum of contributions induced by the first-order Newtonian gauge perturbations Ψ , Φ , v and the synchronous gauge density δ_m^{syn} . Going to Fourier space and using the plane-wave expansion, some of the basic building blocks are, for instance,

$$\Delta_{\ell m}^\Phi = \frac{i^\ell}{2\pi^2} \int d^3 k T_\Phi(k, \chi) j_\ell(k\chi) Y_\ell^{m*}(\hat{\mathbf{k}}) \Phi_i(\mathbf{k}) \quad (\text{A33})$$

$$\Delta_{\ell m}^{v-\hat{\mathbf{n}}} = \frac{i^\ell}{2\pi^2} \int d^3 k T_v(k, \chi) j'_\ell(k\chi) Y_\ell^{m*}(\hat{\mathbf{k}}) \Phi_i(\mathbf{k})$$

$$\Delta_{\ell m}^{\frac{d\bar{\eta}}{d\eta}-\hat{\mathbf{n}}} = -\frac{i^\ell}{2\pi^2} \int d^3 k k T_v(k, \chi) j''_\ell(k\chi) Y_\ell^{m*}(\hat{\mathbf{k}}) \Phi_i(\mathbf{k}).$$

In the second line, the prime denotes a derivative w.r.t. the argument of the spherical bessel function $j_\ell(x)$. Total derivatives w.r.t. the unperturbed conformal time, $d/d\eta \equiv -d/d\chi$, bring an additional derivative w.r.t. the argument of $j_\ell(x)$.

Collecting all the terms and substituting into Eq. (A31), we eventually arrive at

$$a_{\ell m}(\nu) = \frac{i^\ell}{2\pi^2} \int d^3 k \int dz \left(\frac{d\chi}{dz} \right) a(z) \bar{j}_\nu(z) \\ \times F_\ell(\nu, k, z) Y_\ell^{m*}(\hat{\mathbf{k}}) \Phi_i(\mathbf{k}). \quad (\text{A34})$$

The radial window function $F_\ell(\nu, k, z)$ sourced by the perturbations δ_j^N , $\delta \eta$ and δ_\parallel is given by Eq. (27).

For the lensing magnification effect, which is not included in the Fisher analysis as it is small, $F_\ell(\nu, k, z)$ reads

$$F_\ell(\nu, k, z) = \left\{ j_\ell(k\chi) \left[\left(\frac{1}{\mathcal{H}\chi} - 1 \right) T_\Psi - T_\Phi \right] + \left(\frac{1}{\mathcal{H}\chi} - 1 \right) \right. \\ \times \int_0^x d\chi' \left[(T_\Psi + T_\Phi) + \frac{1}{\chi} (\dot{T}_\Psi + \dot{T}_\Phi) \right] j_\ell(k\chi') \\ + \frac{1}{2\chi} \int_0^x d\chi' \frac{\chi - \chi'}{\chi'} (T_\Psi + T_\Phi) j_\ell(k\chi') \\ \left. + j'_\ell(k\chi) \left(1 - \frac{1}{\mathcal{H}\chi} \right) T_v \right\} 2s(\chi), \quad (\text{A35})$$

with the magnification bias $s(\chi)$ given by Eq. (16).

REFERENCES

- Abell P. A., et al., 2009
 Agarwal N., Ho S., Shandera S., 2014, JCAP, 1402, 038
 Alonso D., Bull P., Ferreira P. G., Maartens R., Santos M., 2015, Astrophys. J., 814, 145
 Alonso D., Ferreira P. G., 2015, Phys. Rev., D92, 063525
 Baldauf T., Seljak U., Senatore L., Zaldarriaga M., 2011, JCAP, 10, 031
 Bartolo N., Komatsu E., Matarrese S., Riotto A., 2004, Phys. Rept., 402, 103
 Behroozi P. S., Wechsler R. H., Conroy C., 2013, Astrophys. J. Lett., 762, L31
 Berlind A. A., Weinberg D. H., 2002, Astrophys. J., 575, 587
 Broadhurst T. J., Taylor A. N., Peacock J. A., 1995, Astrophys. J., 438, 49
 Camera S., Maartens R., Santos M. G., 2015, Mon. Not. Roy. Astron. Soc., 451, L80
 Camera S., Santos M. G., Maartens R., 2015, Mon. Not. Roy. Astron. Soc., 448, 1035
 Carbone C., Mena O., Verde L., 2010, JCAP, 1007, 020
 Challinor A., Lewis A., 2011, Phys. Rev. D, 84, 043516
 Chen X., 2010, Adv. Astron., 2010, 638979
 Cooray A., Sheth R. K., 2002, Phys. Rept., 372, 1
 Curto A., Casaponsa B., et al. 2016, in preparation
 Curto A., Tucci M., Kunz M., Martinez-Gonzalez E., 2015, Mon. Not. Roy. Astron. Soc., 450, 3778
 Dalal N., Dore O., Huterer D., Shirokov A., 2008, Phys. Rev., D77, 123514
 de Putter R., Doré O., 2014
 Desjacques V., Chluba J., Silk J., de Bernardis F., Doré O., 2015, Mon. Not. R. Astron. Soc., 451, 4460
 Desjacques V., Seljak U., 2010, Classical and Quantum Gravity, 27, 124011
 Desjacques V., Seljak U., Iliev I. T., 2009, Mon. Not. R. Astron. Soc., 396, 85
 Errard J., Feeney S. M., Peiris H. V., Jaffe A. H., 2016, JCAP, 3, 052
 Gangui A., Lucchin F., Matarrese S., Mollerach S., 1994, Astrophys. J., 430, 447
 Giannantonio T., Ross A. J., Percival W. J., Crittenden R., Bacher D., Kilbinger M., Nichol R., Weller J., 2014, Phys. Rev., D89, 023511

- Hall A., Bonvin C., Challinor A., 2013, *Phys. Rev.*, D87, 064026
- Hall N. R., Keisler R., Knox L., Reichardt C. L., et al. 2010, *Astrophys. J.*, 718, 632
- Hamaus N., Seljak U., Desjacques V., 2011, *Phys. Rev.*, D84, 083509
- Jeong D., Komatsu E., 2009, *Astrophys. J.*, 703, 1230
- Jeong D., Schmidt F., Hirata C. M., 2012, *Phys. Rev.*, D85, 023504
- Knox L., Cooray A., Eisenstein D., Haiman Z., 2001, *Astrophys. J.*, 550, 7
- Kogut A., Chuss D. T., Dotson J., Dwek E., Fixsen D. J., Halpern M., Hinshaw G. F., Meyer S., Moseley S. H., Seifert M. D., Spergel D. N., Wollack E. J., 2014, in *Space Telescopes and Instrumentation 2014: Optical, Infrared, and Millimeter Wave* Vol. 9143 of *Proc. SPIE, The Primordial Inflation Explorer (PIXIE)*. p. 91431E
- Komatsu E., 2010, *Class. Quant. Grav.*, 27, 124010
- Kravtsov A. V., Berlind A. A., Wechsler R. H., Klypin A. A., Gottloeber S., Allgood B., Primack J. R., 2004, *Astrophys. J.*, 609, 35
- Laureijs R., et al., 2011
- Leistedt B., Peiris H. V., Roth N., 2014, *Phys. Rev. Lett.*, 113, 221301
- Liguori M., Sefusatti E., Fergusson J. R., Shellard E. P. S., 2010, *Adv. Astron.*, 2010, 980523
- Linde A., Mukhanov V., 1997, *Phys. Rev. D*, 56, 535
- Lo Verde M., Miller A., Shandera S., Verde L., 2008, *Journal of Cosmology and Astro-Particle Physics*, 4, 14
- Lucchin F., Matarrese S., 1988, *Astrophys. J.*, 330, 535
- Lyth D. H., Ungarelli C., Wands D., 2003, *Phys. Rev. D*, 67, 023503
- Matarrese S., Verde L., 2008, *Astrophys. J.*, 677, L77
- Matarrese S., Verde L., Jimenez R., 2000, *Astrophys. J.*, 541, 10
- Matsumura T., Akiba Y., Borrill J., Chinone Y., Dobbs M., Fuke H., Ghribi A., Hasegawa M., Hattori K., et al. 2014, *Journal of Low Temperature Physics*, 176, 733
- Miville-Deschênes M.-A., Lagache G., Boulanger F., Puget J.-L., 2007, *Astron. Astrophys.*, 469, 595
- Navarro J. F., Frenk C. S., White S. D. M., 1997, *Astrophys. J.*, 490, 493
- Planck Collaboration X 2015, *ArXiv* 1502.01588
- Planck Collaboration XIII 2015, *ArXiv* 1502.01589
- Planck Collaboration XLVIII 2016, *ArXiv* 1605.09387
- Planck Collaboration XVI 2014, *Astron. Astrophys.*, 571, A16
- Planck Collaboration XVII 2015, *ArXiv* 1502.01592
- Planck Collaboration XVIII 2011, *Astron. Astrophys.*, 536, A18
- Planck Collaboration XVIII 2014, *Astron. Astrophys.*, 571, A18
- Planck Collaboration XX 2015, *ArXiv* 1502.02114
- Planck Collaboration XXII 2015, *Astron. Astrophys.*, 576, A107
- Planck Collaboration XXX 2014, *Astron. Astrophys.*, 571, A30
- Planck Collaboration XXX 2016, *Astron. Astrophys.*, 586, A133
- Raccanelli A., et al., 2015, *JCAP*, 1501, 042
- Raccanelli A., Shiraiishi M., Bartolo N., Bertacca D., Liguori M., Matarrese S., Norris R. P., Parkinson D., 2015
- Salopek D. S., Bond J. R., 1990, *Phys. Rev.*, D42, 3936
- Scherrer R. J., Bertschinger E., 1991, *Astrophys. J.*, 381, 349
- Scoccimarro R., Sefusatti E., Zaldarriaga M., 2004, *Phys. Rev.*, D69, 103513
- Scoccimarro R., Sheth R. K., Hui L., Jain B., 2001, *Astrophys. J.*, 546, 20
- Sefusatti E., Komatsu E., 2007, *Phys. Rev.*, D76, 083004
- Seljak U., 2000, *Mon. Not. R. Astron. Soc.*, 318, 203
- Seljak U., 2009, *Physical Review Letters*, 102, 021302
- Shang C., Haiman Z., Knox L., Oh S. P., 2012, *Mon. Not. R. Astron. Soc.*, 421, 2832
- Slosar A., Hirata C., Seljak U., Ho S., Padmanabhan N., 2008, *JCAP*, 0808, 031
- Song Y.-S., Cooray A., Knox L., Zaldarriaga M., 2003, *Astrophys. J.*, 590, 664
- Stivoli F., Grain J., Leach S. M., Tristram M., Baccigalupi C., Stompor R., 2010, *Mon. Not. R. Astron. Soc.*, 408, 2319
- Stompor R., Leach S., Stivoli F., Baccigalupi C., 2009, *Mon. Not. R. Astron. Soc.*, 392, 216
- Tegmark M., 1998, *Astrophys. J.*, 502, 1
- Tegmark M., Eisenstein D. J., Hu W., de Oliveira-Costa A., 2000, *Astrophys. J.*, 530, 133
- Tinker J. L., Kravtsov A. V., Klypin A., Abazajian K., Warren M. S., Yepes G., Gottloeber S., Holz D. E., 2008, *Astrophys. J.*, 688, 709
- Tinker J. L., Robertson B. E., Kravtsov A. V., Klypin A., Warren M. S., Yepes G., Gottloeber S., 2010, *Astrophys. J.*, 724, 878
- Tinker J. L., Wetzel A. R., 2010, *Astrophys. J.*, 719, 88
- Tucci M., Martínez-González E., Vielva P., Delabrouille J., 2005, *Mon. Not. R. Astron. Soc.*, 360, 935
- Viero M. P., Wang L., Zemcov M., Addison G., Amblard A., Arumugam V., Aussel H., Béthermin M., Bock J. e. a., 2013, *Astrophys. J.*, 772, 77
- Yadav A. P. S., Wandelt B. D., 2010, *Adv. Astron.*, 2010, 565248
- Zehavi I., Zheng Z., Weinberg D. H., Blanton M. R., Bahcall N. A., Berlind A. A., Brinkmann J., Frieman J. A., Gunn J. E., Lupton R. H., Nichol R. C., Percival W. J., Schneider D. P., Skibba R. A., Strauss M. A., Tegmark M., York D. G., 2011, *Astrophys. J.*, 736, 59
- Zheng Z., Berlind A. A., Weinberg D. H., Benson A. J., Baugh C. M., Cole S., Dave R., Frenk C. S., Katz N., Lacey C. G., 2005, *Astrophys. J.*, 633, 791